



Titulació:

Màster en Enginyeria Aeronàutica

Alumne:

Èric Godayol Capdevila

Títol TFM:

*Study for the numerical resolution of combustion phenomena in burners*

Director TFM:

Asensio Oliva Llena

Co-Director TFM:

Jordi Ventosa Molina

Convocatòria de lliurament del TFM:

17/06/2016

Contingut d'aquest volum:

**DOCUMENT - MEMÒRIA I ANNEXES**

---

## Abstract

Combustion is a complex phenomenon of interest that combines chemical reactions and turbulent flows. Resolution of both problems is a difficult task. On the one hand, chemical reactions introduce a large amount of species with different properties and small temporal scales due to chemical kinetics. On the other hand, turbulent flows imply a large span of spatial scales.

Different models are commonly applied to reduce these requirements. Chemical reactions can be modeled with reduced chemical mechanisms. These have less species and reactions than complex ones, but are able to describe the combustion. Turbulence is modeled by means of Large Eddy Simulation (LES), which filters the Navier-Stokes equations spatially. Thus, the small scales of the flow are filtered out. These ones are modeled through a turbulent viscosity.

The present study focuses on the theoretical basis required to model combustion phenomena. First, the algorithm used to solve variable density flows is presented. It uses the low-Mach equations, which are discretized in terms of the convective-diffusive equation. Its resolution is achieved by applying an algorithm based on a projection method, using a predictor-corrector step. Then the algorithm used to solve chemical kinetics is detailed. In this case, the Arrhenius law is used for laminar flames and a two equations model for turbulent flows. The latter introduces an eddy dissipation model besides the Arrhenius law to include the effect of the filtered spatial scales in LES simulations. The study concludes with an introduction to LES. The spatial filter introduces some additional terms in the governing equations. These ones are modeled through a turbulent viscosity. Different models to evaluate the turbulent viscosity can be found in the literature. In the present study the Smagorinsky model is used.

Different tests are carried out to verify the results. The lid driven cavity and the heated cavity tests show that accurate results are obtained for incompressible and variable density non-reacting flows. A laminar methane/air flame test is used to verify the laminar chemical algorithm. Additionally, the influence of chemical mechanism on the flame behavior is shown. Finally, a three dimensional propane burner is simulated to study the turbulent combustion phenomena and verify the interaction between turbulent combustion chemical algorithm and LES.

An additional test is used to assess the speedup of the parallelization implemented and also to check its performance.

# Table of Contents

<b>1. INTRODUCTION.....</b>	<b>1</b>
1.1. OBJECTIVE .....	1
1.2. JUSTIFICATION.....	1
1.3. SCOPE .....	2
1.4. BASIC SPECIFICATIONS.....	2
<b>2. LOW MACH NUMBER EQUATIONS.....</b>	<b>3</b>
2.1. INTRODUCTION .....	3
2.2. GOVERNING EQUATIONS.....	4
2.2.1. Projection Method .....	5
2.3. DOMAIN DISCRETIZATION.....	6
2.3.1. Convection – Diffusion Equation .....	6
2.3.2. Numerical Schemes .....	8
2.3.3. Implementation Scheme .....	10
2.3.4. Boundaries .....	11
2.4. TEMPORAL DISCRETIZATION.....	12
2.4.1. Predictor Step.....	12
2.4.2. Corrector Step .....	13
2.4.3. Stability .....	14
2.5. VERIFICATION.....	15
2.5.1. Test – Driven Cavity .....	15
2.5.2. Test – Heated Cavity.....	17
2.5.3. Test – Parallel Execution .....	21
<b>3. REACTING FLOWS .....</b>	<b>22</b>
3.1. INTRODUCTION .....	22
3.2. SPECIES CHARACTERIZATION.....	23
3.2.1. Thermochemistry.....	23
3.2.2. Chemical Kinetics.....	24
3.2.1. Thermodynamic Properties .....	25
3.3. CHEMICAL MODELS .....	26
3.3.1. Single Step CH <sub>4</sub> / Air Model .....	26
3.3.2. Four Step CH <sub>4</sub> / Air Model .....	27
3.4. GOVERNING EQUATIONS.....	29
3.4.1. Species Conservation .....	29
3.4.2. Energy Conservation.....	30
3.4.3. Radiation .....	31
3.5. TEMPORAL DISCRETIZATION.....	33
3.5.1. Predictor Step.....	33
3.5.2. Corrector Step .....	33
3.5.3. Stability .....	34
3.6. LAMINAR FLAMES .....	35

3.6.1.	Premixed Flames .....	35
3.6.2.	Non Premixed Flames.....	37
3.7.	VERIFICATION – PREMIXED FLAMES.....	38
3.7.1.	Test – Single Step <b>CH<sub>4</sub></b> / Air Model .....	39
3.7.2.	Test – Four Steps <b>CH<sub>4</sub></b> / Air Model .....	45
<b>4.</b>	<b>TURBULENCE MODELLING.....</b>	<b>51</b>
4.1.	INTRODUCTION .....	51
4.2.	LARGE – EDDY SIMULATION .....	52
4.2.1.	Temporal Average.....	52
4.2.2.	LES Equations.....	54
4.2.3.	Smagorinsky Model.....	55
4.3.	EDDY DISSIPATION COMBUSTION .....	56
4.3.1.	Single Step <b>C<sub>3</sub>H<sub>8</sub></b> / Air Model .....	57
4.4.	APPLICATION.....	58
4.4.1.	<b>C<sub>3</sub>H<sub>8</sub></b> / Air Non-premixed Burner .....	58
<b>5.</b>	<b>SCHEDULE.....</b>	<b>65</b>
5.1.	TASK DESCRIPTION .....	65
5.2.	GANTT DIAGRAM .....	68
<b>6.</b>	<b>ENVIRONMENTAL IMPACT .....</b>	<b>70</b>
<b>7.</b>	<b>BUDGET .....</b>	<b>71</b>
<b>8.</b>	<b>CONCLUSIONS.....</b>	<b>72</b>
<b>9.</b>	<b>FURTHER DEVELOPMENTS .....</b>	<b>73</b>
	<b>BIBLIOGRAPHY .....</b>	<b>74</b>
	<b>APPENDIX A – COEFFICIENTS FOR THERMODYNAMIC PROPERTIES .....</b>	<b>76</b>

## Table of Tables

<b>Table 1.</b> Coefficients for different numerical schemes, where subscript $f$ represents the face where variable $\phi$ is defined and $Ff$ represents the mass flow through face $f$ . .....	10
<b>Table 2.</b> Comparison of Nusselt numbers and thermodynamic pressure of different schemes and reference values. ....	19
<b>Table 3.</b> Mass fractions for reactants at stoichiometric conditions. ....	26
<b>Table 4.</b> Mass fractions for products at stoichiometric conditions. ....	26
<b>Table 5.</b> Coefficients applied on the Arrhenius equation. ....	27
<b>Table 6.</b> Coefficients applied on the rate of progress computation. ....	27
<b>Table 7.</b> Molar mass of species involved on the simple step mechanism. ....	27
<b>Table 8.</b> Coefficients applied on the Arrhenius equation. ....	28
<b>Table 9.</b> Coefficients applied on the rate of progress computation. ....	28
<b>Table 10.</b> Coefficients applied on the backward rate of progress computation. ....	28
<b>Table 11.</b> Molar mass of added species on the four step mechanism. ....	28
<b>Table 12.</b> Lewis number for different species used on computations. ....	29
<b>Table 13.</b> Coefficients applied on the Arrhenius equation. ....	57
<b>Table 14.</b> Coefficients applied on the EDM equation. ....	57
<b>Table 15.</b> Molar mass of added species on the four step mechanism. ....	57
<b>Table 16.</b> Estimation of hours per task scheduled. ....	68
<b>Table 17.</b> Cost per resource and final budget of the study. ....	71
<b>Table 18.</b> Methane (CH <sub>4</sub> ) coefficients from 200 - 1000 K. ....	76
<b>Table 19.</b> Methane (CH <sub>4</sub> ) coefficients from 1000 - 5000 K. ....	76
<b>Table 20.</b> Oxygen (O <sub>2</sub> ) coefficients from 200 - 1000 K. ....	76
<b>Table 21.</b> Oxygen (O <sub>2</sub> ) coefficients from 1000 - 5000 K. ....	76
<b>Table 22.</b> Carbon Monoxide (CO) coefficients from 200 - 1000 K. ....	76
<b>Table 23.</b> Carbon Monoxide (CO) coefficients from 1000 - 5000 K. ....	77
<b>Table 24.</b> Carbon dioxide (CO <sub>2</sub> ) coefficients from 200 - 1000 K. ....	77
<b>Table 25.</b> Carbon dioxide (CO <sub>2</sub> ) coefficients from 1000 - 5000 K. ....	77
<b>Table 26.</b> Water (H <sub>2</sub> O) coefficients from 200 - 1000 K. ....	77
<b>Table 27.</b> Water (H <sub>2</sub> O) coefficients from 1000 - 5000 K. ....	77
<b>Table 28.</b> Hydrogen (H <sub>2</sub> ) coefficients from 200 - 1000 K. ....	77
<b>Table 29.</b> Hydrogen (H <sub>2</sub> ) coefficients from 1000 - 5000 K. ....	77
<b>Table 30.</b> Nitrogen (N <sub>2</sub> ) coefficients from 200 - 1000 K. ....	78
<b>Table 31.</b> Nitrogen (N <sub>2</sub> ) coefficients from 1000 - 5000 K. ....	78
<b>Table 32.</b> Coefficients for all species used on the entropy equation for 200 – 100 K (1) and 1000 – 5000 K (2). ....	78

## Table of Figures

<b>Figure 1.</b> Staggered volume of velocity with collocated volumes of scalar variables (1D). .....	7
<b>Figure 2.</b> Staggered volume of velocity $u$ and vertical velocities used to compute the mass flow through the upper face. ....	8
<b>Figure 3.</b> Geometry and boundary conditions for the lid driven cavity problem. .	15
<b>Figure 4.</b> Vertical $vX$ profile at $x = 0.5$ (left) and horizontal $vy$ profile at $y = 0.5$ (right) for the lid driven cavity at $Re = 3200$ using a $128 \times 128$ control volumes (CV) mesh. ....	16
<b>Figure 5.</b> Velocity field of the lid driven cavity at $Re = 3200$ using a $128 \times 128$ CV mesh (left) and reference stream lines from Ghia et. al. [8] (right).....	16
<b>Figure 6.</b> Geometry and boundary conditions for the heated cavity problem. ....	17
<b>Figure 7.</b> Vertical $u$ profile at $x = 0.5$ (top – left), horizontal $v$ profile at $y = 0.5$ (top – right), temperature profile at $x = 0.5$ (bottom – left) and temperature profile at $y = 0.5$ (bottom – right) using a $128 \times 128$ CV mesh. ....	18
<b>Figure 8.</b> Velocity field of the heat cavity at $Ra = 106$ using a $128 \times 128$ CV mesh (left) and reference stream lines from Vierendeels et. al. [9] (right). ....	19
<b>Figure 9.</b> Temperature field of the heat cavity at $Ra = 106$ and $128 \times 128$ mesh (left) and reference contours from Vierendeels et. al. [9] (right).....	19
<b>Figure 10.</b> Computational scalability and number of threads (Heated cavity at $Ra = 106$ and $\varepsilon = 0.6$ using a $128 \times 128$ CV mesh).....	21
<b>Figure 11.</b> Geometry of the burner used on premixed laminar flames. ....	38
<b>Figure 12.</b> Geometry and refined grid of $90 \times 180$ CV.....	39
<b>Figure 13.</b> Temperature of a single premixed $CH_4$ /Air using a $90 \times 180$ control volumes (CV) refined mesh. ....	40
<b>Figure 14.</b> Temperature contours of 38 reactions and 14 species mechanism from Fiorina et. al. [14]. ....	40
<b>Figure 15.</b> Streamlines of single step premixed $CH_4$ /Air using a $90 \times 180$ CV refined mesh. ....	41
<b>Figure 16.</b> Rates of production (left) and mass fractions related with temperature (right) through $Y$ for a single step premixed $CH_4$ /Air using a $90 \times 180$ CV refined mesh.....	41
<b>Figure 17.</b> Radial profiles of temperature and mass fractions of $H_2O$ and $CO_2$ at $y = 0.003$ for a single step premixed $CH_4$ /Air using a $90 \times 180$ CV refined mesh. ....	42
<b>Figure 18.</b> Radial profiles of temperature and mass fractions of $H_2O$ and $CO_2$ at $y = 0.007$ for a single step premixed $CH_4$ /Air using a $90 \times 180$ CV refined mesh. ....	42

<b>Figure 19.</b> Radial profiles of temperature and mass fractions of $H_2O$ and $CO_2$ at $y = 0.011$ for a single step premixed $CH_4$ /Air using a $90 \times 180$ CV refined mesh.	43
<b>Figure 20.</b> Mass fractions for a single step premixed $CH_4$ /Air using a $90 \times 180$ CV refined mesh ( $CH_4$ -left and $CO_2$ -right).	43
<b>Figure 21.</b> Mass fractions for a single step premixed $CH_4$ /Air using a $90 \times 180$ CV refined mesh ( $O_2$ -left and $H_2O$ -right).	44
<b>Figure 22.</b> Temperature of four step premixed $CH_4$ /Air using a $90 \times 180$ CV refined mesh.	45
<b>Figure 23.</b> Streamlines of four step premixed $CH_4$ /Air using a $90 \times 180$ CV refined mesh.	46
<b>Figure 24.</b> Rates of production (left) and mass fractions related with temperature (right) through Y of a four step premixed $CH_4$ /Air using a $90 \times 180$ CV refined mesh.	46
<b>Figure 25.</b> Radial profiles of temperature and mass fractions of $H_2O$ and $CO_2$ at $y = 0.003$ of four step (lines) and single step (dots) premixed $CH_4$ /Air using a $90 \times 180$ CV refined mesh.	47
<b>Figure 26.</b> Radial profiles of temperature and mass fractions of $H_2O$ and $CO_2$ at $y = 0.007$ of four step (lines) and single step (dots) premixed $CH_4$ /Air using a $90 \times 180$ CV refined mesh.	47
<b>Figure 27.</b> Radial profiles of temperature and mass fractions of $H_2O$ and $CO_2$ at $y = 0.011$ of four step (lines) and single step (dots) premixed $CH_4$ /Air using a $90 \times 180$ CV refined mesh.	48
<b>Figure 28.</b> Mass fractions for a four step premixed $CH_4$ /Air using a $90 \times 180$ CV refined mesh ( $CH_4$ -left and $CO_2$ -right).	49
<b>Figure 29.</b> Mass fractions for a four step premixed $CH_4$ /Air using a $90 \times 180$ CV refined mesh ( $CO$ -left and $H_2$ -right).	49
<b>Figure 30.</b> Mass fractions for a four step premixed $CH_4$ /Air using a $90 \times 180$ CV refined mesh ( $O_2$ -left and $H_2O$ -right).	50
<b>Figure 31.</b> Geometry of the burner used on the turbulent non premixed flame.	58
<b>Figure 32.</b> Three dimensional view of the domain that defines the propane burner.	59
<b>Figure 33.</b> Mean reaction rates contours ( $kg/m^3s$ ) of propane for turbulent $C_3H_8$ /Air using a $166 \times 100 \times 20$ CV mesh.	59
<b>Figure 34.</b> Mean reaction rates contours at the middle plane (each $0.25 kg/m^3s$ from 0 to $3 kg/m^3s$ ) with Wale model ( $125 \times 100 \times 15$ CV the first one and $166 \times 100 \times 20$ CV the second one) from Howard et. al. [17].	60
<b>Figure 35.</b> Mean temperature (K) for turbulent $C_3H_8$ /Air using a $166 \times 100 \times 20$ CV mesh.	60

<b>Figure 36.</b> Mean mass fraction of propane for turbulent $C_3H_8$ /Air using a $166 \times 100 \times 20$ CV mesh. ....	60
<b>Figure 37.</b> Mean mass fraction of oxygen for turbulent $C_3H_8$ /Air using a $166 \times 100 \times 20$ CV mesh. ....	61
<b>Figure 38.</b> Mean mass fraction vertical profiles of oxygen using the Smagorinsky model (line) at $x = 0.04$ and $x = 0.12$ m for turbulent $C_3H_8$ /Air using a $166 \times 100 \times 20$ CV mesh. ....	61
<b>Figure 39.</b> Mean profiles of horizontal velocity using the Smagorinsky model (line) at $x = 0.04$ m and $x = 0.12$ m for turbulent $C_3H_8$ /Air using a $166 \times 100 \times 20$ CV mesh. ....	62
<b>Figure 40.</b> Instantaneous field of temperature (K) and rate of production contours (top) and stoichiometric mixture fraction contours $Z_{st} \pm 0.01$ (bottom) for turbulent $C_3H_8$ /Air using a $166 \times 100 \times 20$ CV mesh. ....	62
<b>Figure 41.</b> Instantaneous field of propane mass fraction and rate of production contours for turbulent $C_3H_8$ /Air using a $166 \times 100 \times 20$ CV mesh (SP on top and UDS on bottom). ....	63
<b>Figure 42.</b> Instantaneous field of oxygen mass fraction and rate of production contours for turbulent $C_3H_8$ /Air using a $166 \times 100 \times 20$ CV mesh (SP on top and UDS on bottom). ....	63
<b>Figure 43.</b> Gantt Diagram. ....	69



# Nomenclature

$\gamma$	Adiabatic index
$M$	Mach number
$\rho$	Density [ $kg/m^3$ ]
$x_i$	$i$ – coordinate [ $m$ ]
$\delta x_i$	$i$ – direction distance between two adjacent nodes
$\Delta x_i$	$i$ – direction width of the control volume
$\vec{u}$	Velocity vector [ $m/s$ ]
$u_i$	$i$ – direction velocity [ $m/s$ ]
$u$	$x$ – direction velocity [ $m/s$ ]
$v$	$y$ – direction velocity [ $m/s$ ]
$w$	$z$ – direction velocity [ $m/s$ ]
$t$	Time [ $s$ ]
$\Delta t$	Time – step [ $s$ ]
$\mu$	Dynamic viscosity [ $kg/(m \cdot s)$ ]
$\mu_t$	Turbulent dynamic viscosity [ $kg/(m \cdot s)$ ]
$\lambda$	Thermal conductivity [ $W/(m \cdot K)$ ]; wave length [ $m$ ] in section 3.4.3
$\lambda_t$	Turbulent thermal conductivity [ $W/(m \cdot K)$ ]
$\delta_{ij}$	Dirac delta function
$P_0$	Thermodynamic pressure [ $Pa$ ]
$p$	Dynamic pressure [ $Pa$ ]
$\vec{g}$	Gravity [ $m/s^2$ ]
$h$	Enthalpy [ $J/(kg)$ ]
$h_s$	Sensible enthalpy [ $J/(kg)$ ]
$\Delta h_f^0$	Formation enthalpy [ $J/(kg)$ ]
$T$	Temperature [ $K$ ]

$C_p$	Heat capacity at constant pressure [ $J/(kg \cdot K)$ ]
$R$	Gas constant [ $J/(mol \cdot K)$ ]
$R_g$	Gas constant for specific species [ $J/(kg \cdot K)$ ]
$M_0$	Total mass in a closed cavity [ $kg$ ]
$A$	Area [ $m^2$ ]
$V$	Volume [ $m^3$ ]
$\phi$	General dependent variable
$T$	Diffusive constant in the convection-diffusion equation
$S$	Source term in the convection-diffusion equation
$F$	Flow rate through a cell face in the convection-diffusion equation [ $kg/s$ ]
$D$	Diffusive coefficient in the convection-diffusion equation
$P_e$	Peclet number
$A_{1,2}$	Convection-diffusion coefficients
$a$	Coefficients in the discretized convection-diffusion equation
$Re$	Reynolds number
$\varepsilon$	Non – dimensional temperature difference
$Ra$	Rayleigh number
$Pr$	Prandtl number
$Pr_t$	Turbulent Prandtl number
$Y_k$	Mass fraction of species $k$
$W$	Molecular weight [ $kg/mol$ ]
$\nu'_{kj}$	Reactant stoichiometric coefficient of species $k$ in reaction $j$
$\nu''_{kj}$	Product stoichiometric coefficient of species $k$ in reaction $j$
$\nu_{kj}$	Global stoichiometric coefficient of species $k$ in reaction $j$
$Q_j$	Rate of progress of reaction $j$ [ $mol/(L \cdot s)$ ]
$Kf_j$	Forward reaction constant
$Kr_j$	Reverse reaction constant

$A_j$	Pre-exponential factor of reaction $j$ in Arrhenius law
$\beta$	Temperature exponent of reaction $j$ in Arrhenius law
$Ea$	Activation Energy [ $J/kg$ ]
$\dot{\omega}_k$	Rate of production of species $k$ [ $kg/(m^3 \cdot s)$ ]
$V_{k,i}$	$i$ – direction molecular diffusive velocity of species $k$
$Le_k$	Lewis number of species $k$
$D_k$	Molecular diffusivity coefficient [ $m^2/s$ ]
$D_{kt}$	Turbulent molecular diffusivity coefficient [ $m^2/s$ ]
$\dot{\omega}_T$	Heat release [ $J/(m^3 \cdot s)$ ]
$\vec{q}^R$	Radiation energy [ $J/(m^2 \cdot s)$ ]
$\delta$	Premixed flame diffusive thickness [m]
$\delta_L^b$	Premixed flame thickness from Blint correlation [m]
$S_L$	Flame speed [ $m/s$ ]
$Sc$	Schmidt number
$Sc_t$	Turbulent Schmidt number
$A_{EDM}$	Combustion model constant
$\bar{\kappa}$	Subgrid turbulent kinetic energy [ $kg \cdot m^2/s^2$ ]
$C_k$	Kolmogorov constant
$C_s$	Turbulence model constant
$\mu_{EDM}$	Dynamic viscosity in eddy dissipation model [ $kg/(m \cdot s)$ ]

#### Subscripts

$i$	Direction
$j$	Component in section 2; Reaction in other sections
$k$	Species
$f$	Face of the control volume

# 1. Introduction

## 1.1. Objective

The main objective of this study is to improve the knowledge about combustion theory and apply it to develop a 3D computational fluid dynamics (CFD) code for multispecies and reactive flows, with variable density and properties as a function of temperature.

## 1.2. Justification

The continuous improvement in combustion engines requires new tools to model the complexity behind them with the aim of designing burners that ensure maximum efficiency combined with low pollutant emissions. Efficient combustion chambers have to ensure the maximum combustion efficiency, with minimum pressure drops and no flames through the outlet. Moreover, other design features are introduced to make them safe, and also ensure flame stabilization through a large range of pressures and minimize carbon depositions.

In the context of aircraft engines, temperatures are limited in the range of  $700^{\circ}\text{C}$  to  $1200^{\circ}\text{C}$  to avoid thermomechanical failure on turbine blades and nozzles.

The accomplishment of all these requirements is a hard task that takes several years of design and experimentation. The introduction of CFD in this field is used to simulate entire engines and reduce costs of development and experimentation. In addition, the application of CFD codes could increase the knowledge about the combustion process inside burners and ease the optimization task.

Typically combustions occurs under turbulent conditions. Resolution of both problems becomes a difficult task. On the one hand, chemical reactions introduce a large amount of species, and on the other hand, turbulent flows imply complex flow patterns.

The resolution of simple cases with turbulent reacting flows is a first step toward more complex ones, which will provide the theoretical basis to understand the combustion process and extend it to aeronautical application cases.

## 1. INTRODUCTION

---

### 1.3. Scope

The main scope of the present study is to improve the knowledge about combustion theory and develop a code to simulate combustion processes. The objectives that ensure the achievement of the main scope are the following ones:

- Develop a three dimensional CFD code to simulate simple burner geometries.
- Work on the low-Mach equations and the finite volume method to study variable density flows.
- Work on the multispecies theory and implement it to the CFD code, introducing the species transport equation and variable thermodynamic properties as a function of temperature and species mass fractions.
- Work on the chemical mechanisms to compute reversible reactions and multistep chemical mechanisms.
- Work on the turbulent combustion models and implement a basic LES model.

### 1.4. Basic Specifications

Basic specifications of the developed code are detailed:

- The CFD code only can be applied over uniform structured meshes.
- Five numerical schemes are implemented, four of low order and one of high order.
- Range of application of the CFD code developed is limited to incompressible and low-Mach flows.
- Only Newtonian flows are allowed to be introduced on the CFD code, which means that viscosity only depends on temperature and thermodynamic pressure.
- Combustion processes must include a diluent species, as nitrogen, to absorb all the inconsistencies introduced by Fick's law.
- Radiation effects are not taken into account.
- Simple chemical mechanisms without molecular collisions are implemented.

## 2. Low Mach number Equations

### 2.1. Introduction

Different approaches to solve incompressible and compressible flows have been developed over the last century. In the past decades, flows at low-Mach numbers and also variable density have attracted a lot of interest due to its potential on different fields of study, as natural phenomena and technological processes. Some examples could be the study of meteorological flows, flows with high mass and/or heat transfers, and also premixed and diffusion flames.

Explicit compressible schemes without any modification become impractical to solve flows for Mach numbers near 0, and incompressible schemes are not able to provide accurate results when high heat transfer occurs on the flow [1]. In these cases, the best option is to use the low-Mach equations. These ones are obtained from the compressible formulation by expanding the flow variables of the governing equations as power series of  $\gamma M^2$  [2].

This chapter focuses on the low-Mach flow Navier-Stokes equations. The spatial discretization over the computational domain and the temporal discretization applied on the convection-diffusion equation are presented, with the numerical schemes and the algorithm of resolution. At the end are exposed different tests which are used to verify the developed code.

### 2.2. Governing Equations

The governing equations for low-Mach flows, which are obtained from the compressible ones, are exposed below<sup>1</sup>.

$$\frac{\partial \rho}{\partial t} = -\frac{\partial(\rho u_j)}{\partial x_j} \quad (2.1)$$

$$\frac{\partial(\rho u_i)}{\partial t} = -\frac{\partial(\rho u_j u_i)}{\partial x_j} - \frac{\partial p}{\partial x_i} + \frac{\partial \tau_{ij}}{\partial x_j} + \rho g_i \quad (2.2)$$

$$\rho \frac{\partial h}{\partial t} = -\rho u_j \frac{\partial h}{\partial x_j} + \frac{dP_0}{dt} - \frac{\partial \dot{q}_j}{\partial x_j} \quad (2.3)$$

where  $\tau_{ij} = \mu \left( \frac{\partial u_i}{\partial x_j} + \frac{\partial u_j}{\partial x_i} - \frac{2}{3} \delta_{ij} \frac{\partial u_k}{\partial x_k} \right)$  and  $\dot{q}_j = -\lambda \frac{\delta T}{\delta x_j}$ , which correspond to the application of Stokes' law and Fourier's law. As it can be seen on the momentum ( 2.2 ) and energy ( 2.3 ) equations, two different pressures are defined. The first one is the dynamic pressure ( $p$ ), and the second one the thermodynamic pressure ( $P_0$ ). The latter is related with the density through the state equation of an ideal gas.

$$P_0 = \rho RT \quad (2.4)$$

The evolution over time of the thermodynamic pressure depends on the case of study. In general, two cases of interest are identified [2].

- Open Cavity: Thermodynamic pressure is constant and equal to the boundary thermodynamic pressure.
- Closed Cavity: Thermodynamic pressure depends on the density and temperature of the volume. Taking in account that the total mass remains constant and applying the state equation, one can obtain a general form to compute it for a given mass and temperature.

$$P_0 = \frac{M_0 \cdot R_g}{\int \frac{dV}{T}} \quad (2.5)$$

<sup>1</sup> Full demonstration of the low-Mach number Navier-Stokes equations can be found on Lessani and Papalexandris [2].

where the mass of the cavity is computed using the initial conditions.

$$M_0 = \frac{P_0}{R_g} \cdot \int \frac{dV}{T_{t_0}} \quad (2.6)$$

For non-reacting flows, temperature is recovered from the definition of the sensible enthalpy.

$$dh = c_p dT \quad (2.7)$$

It is interesting to note that due to the low Mach condition, the viscosity and pressure terms on the energy equation ( 2.3 ) are smaller enough to be neglected. Moreover the energy equation is in non-conservative form because density is computed after it, which on explicit schemes implies that energy conservation and state equation of an ideal gas cannot be accomplished simultaneously.

### 2.2.1. Projection Method

To solve the pressure-velocity coupling a projection method is proposed. The projection method is based on the definition of a new vector field that corresponds to a velocity field, known as pseudo velocity, without the condition of mass conservation.

$$\nabla \cdot (\rho u_p) = \nabla \cdot (\rho u) - \nabla^2 p \quad (2.8)$$

In incompressible flows, mass divergence is null ( $\nabla(\rho u) = 0$ ). On variable density flows, this term cannot be simplified since its value is not known. Usually it is replaced with the density variation over time from the continuity equation ( 2.1 ). Some studies [3] [4] found that this term introduces instabilities into the computation algorithm. To reduce these instabilities a second order approximation is recommended.

$$\frac{\partial \rho}{\partial t} = \frac{((\Delta t^n + \Delta t^{n-1})^2 - (\Delta t^n)^2) \cdot \rho^l - (\Delta t^n + \Delta t^{n-1})^2 \cdot \rho^n + (\Delta t^n)^2 \cdot \rho^{n-1}}{\Delta t^n \cdot \Delta t^{n-1} \cdot (\Delta t^n + \Delta t^{n-1})} \quad (2.9)$$

The full application of the projection method into the algorithm is explained in section 2.4.



### 2.3. Domain Discretization

The governing equations are discretized over the domain by applying the finite volume method. This consists on dividing the domain in different control volumes where the governing equations are applied on its integral form. The discretization must be consistent and stable, which means that the solution of the discretized equations must tend to the solution of the differential ones when the discretization tends to zero.

Two discretization typologies are identified, the structured and the unstructured. The first one shows a constant pattern through the domain, while the second one is completely irregular. In this study the structured discretization is used. It is known that structured discretization are suitable for simple geometries, but dealing with more complex grids and geometries is out of the scope of this study.

#### 2.3.1. Convection – Diffusion Equation

The governing equations are expressed as a single equation, referred as the convective-diffusive equation. The main terms of this equation are identified as temporal, convective, diffusive and source, respectively.

$$\frac{\partial(\rho\phi)}{\partial t} + \nabla \cdot (\rho \vec{v} \phi) = \nabla \cdot (T \cdot \nabla \phi) + S \quad (2.10)$$

where T and S are suitably selected to reconstruct the governing equations.  $\phi$  is the dependent variable, for instance velocity ( $u, v, w$ ) or enthalpy ( $h$ ). The equation is discretized over each control volume, which leads to the following equation<sup>2</sup>.

$$\int_V \frac{\partial(\rho\phi)}{\partial t} dV = - \int_A (\rho \vec{v} \phi) \cdot \vec{n} dA + \int_A (T \cdot \nabla \phi) \cdot \vec{n} dA + \int_V S \cdot dV \quad (2.11)$$

It is important to note that the energy equation is in non-conservative form. This implies a modification of the convective term.

$$\rho u \cdot \nabla h = \nabla \cdot (\rho u h) - h \cdot \nabla \cdot (\rho u) \quad (2.12)$$

The first term on the right hand side corresponds to the convective term in conservative form and the last one is added to the source term.

<sup>2</sup> The divergence theorem, also known as Gauss's theorem relates the flow of a vector field through a surface with the behavior of the vector inside the surface.

$$\int_V \nabla \cdot \vec{u} dV = \int_A \vec{u} \cdot \vec{n} dA$$

The right hand side of the convective-diffusive equation ( 2.11 ) applied on a control volume gives the following discretization.

$$R(\phi) = \sum_i [(-\rho u \phi + T \cdot \nabla \phi)_{f_i} \cdot A_{f_i}] + S \cdot V \quad (2.13)$$

Usually variables are defined at the middle of the control volume, so their values on surfaces are not known. These ones must be estimated with the application of face interpolations, which are explained on section 2.3.2.

At this point it is interesting to introduce the checkerboard problem. The projection method used to decouple the pressure from the velocity field introduces the checkerboard problem when a collocated discretization is used on the domain [5]. This error appears because the resolution of the Poisson equation ensures mass conservation on the cell faces but not on the velocities defined at the center of the cell. With the aim of avoiding this issue, different models can be found in the literature. One of them consists on modifying the velocity computation to keep the collocated discretization. The other one uses a staggered discretization. The latter consists on defining different control volumes for the velocity field. Both of them appear to be equal, with similar results and accuracy [6]. Collocated schemes are more suitable for engineering purposes due to its simplicity when dealing with unstructured discretization. Even so in this study only structured discretization is used, which ease the implementation of staggered grids. Therefore, the staggered grid is able to conserve the kinetic energy with a suitable numerical scheme.

### 2.3.1.1. Staggered Discretization

Staggered discretization defines a set of displaced grids (one per dimension) with the objective to store the velocities on the cell faces of the original grid. This definition is interesting because it ensures mass conservation on the scalar equations and also simplifies the computation of the convective terms.

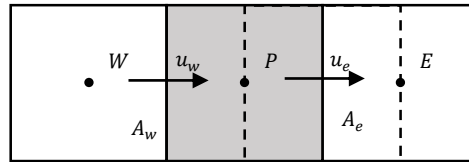


**Figure 1.** Staggered volume of velocity with collocated volumes of scalar variables (1D).

In the present study, the staggered discretization is applied to the velocity field to avoid the checkerboard problem, and the collocated discretization is applied on the scalar fields.

### 2.3.2. Numerical Schemes

As described on the discretization section, some variables need to be interpolated at cell faces, which include gradients, variables and fluid properties.

#### 2.3.2.1. Diffusive Term

The diffusive term of the discretized convection-diffusion equation ( 2.13 ) consists on evaluating the gradient over the faces of the control volume. This is done by a Taylor expansion.

$$\left. \frac{\partial \phi}{\partial x} \right|_e \approx \frac{\phi_E - \phi_P}{\delta x_e} \quad ( 2.14 )$$

It is interesting to note that for structured grids it is a second order approximation, but for refined structured grids, it becomes a first order approximation.

#### 2.3.2.2. Convective Term

The convective term can be split into two parts, the mass flow through the surface and the variable evaluated at the face of the control volume.

Momentum equations are applied to staggered control volumes. This requires the introduction of a second step to compute the mass flow through a face.

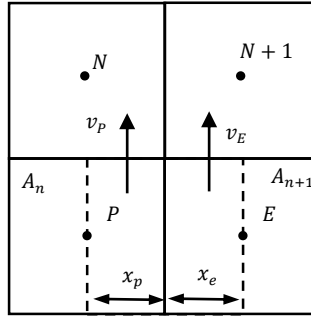


**Figure 2.** Staggered volume of velocity  $u$  and vertical velocities used to compute the mass flow through the upper face.

Densities at the faces are evaluated with a weighted mean. Due to the staggered configuration, two different mass flows are defined on the same face, so the final mass flow is computed as the sum of both values.

$$F_n = \frac{1}{2}(\rho_P + \rho_N) \cdot v_P \cdot x_{i,e} + \frac{1}{2}(\rho_E + \rho_{N+1}) \cdot v_E \cdot x_{i+1,w} \quad ( 2.15 )$$

where  $x_p$  and  $x_e$  represent the area between the staggered and the collocated grid as detailed in **Figure 2**.

### 2.3.2.3. Face Interpolations

The convective term requires a variable defined at the cell face, which is unknown. Therefore interpolation methods must be applied on each face of the control volume.

To preserve the global kinetic energy, it is recommended to use a symmetry-preserving scheme (SP) on the momentum equations. This ensures the preservation of the physical properties of the Navier-Stokes equations deduced from the symmetries of the differential operators and from the convective operator, which imply that the convective term must be skew-symmetric and the diffusive term must be symmetric and positive defined [7].

Even so, other schemes are introduced for the scalar equations. On this study, the central difference scheme (CDS), the upwind scheme (UDS), the hybrid scheme (HDS), the power-law scheme (PLDS) and also the quadratic upstream interpolation for convective kinematics (QUICK) are implemented for the scalar equations [5].

CDS scheme is a second order scheme similar to the SP on structured uniform meshes. This scheme is only accurate for  $Pe < 2$ , where  $Pe$  is the Peclet number that relates the convection term and the diffusion term.

UDS scheme is a first order scheme where the face variable is set to the downstream volume variable. This scheme is useful for high Peclet numbers. Still, it is known that this scheme introduces false diffusivity, which is not desired.

HDS scheme takes advantage of the CDS and UDS scheme. For low values of Peclet (below 2) it applies a CDS scheme, and for higher values, where CDS cannot be used, it applies a UDS scheme.

PLDS scheme uses a fifth order approximation to the analytical solution of the 1D convective – diffusive equation. For values of Peclet higher than 10, the diffusive term is set to 0.

QUICK scheme is the only high order scheme implemented on this work. This scheme uses a three point upstream weighted quadratic interpolation. It takes into account the second order derivative, so it is a three order scheme.

### 2.3.3. Implementation Scheme

The implementation is based on a unique algebraic equation with different coefficients which are suitably selected to get the desired numerical scheme for a structured and uniform mesh [5]. A 1D case is exposed below.

$$R(\phi) = a_E \cdot \phi_E + a_W \cdot \phi_W - a_P \cdot \phi_P + S \cdot V \quad (2.16)$$

where

$$a_E = D_e \cdot A_1 + \max(0, -A_2) \quad (2.17)$$

$$a_W = D_w \cdot A_1 + \max(0, A_2) \quad (2.18)$$

Coefficients  $A_1$  and  $A_2$  are defined on **Table 1**.

**Table 1.** Coefficients for different numerical schemes, where subscript  $f$  represents the face where variable  $\phi$  is defined and  $F_f$  represents the mass flow through face  $f$ .

<b>Numerical Scheme</b>	<b><math>A_1</math></b>	<b><math>A_2</math></b>
<i>CDS</i>	$1 - 0.5 \cdot  Pe_f $	$F_f$
<i>UDS</i>	1	$F_f$
<i>HDS</i>	0	$F_f$
<i>PLDS</i>	$(1 - 0.1 \cdot  Pe_f )^5$	$F_f$
<i>QUICK</i>	$1 - 0.375 \cdot  Pe_f $	$1.125 \cdot F_f + 0.125 \cdot F_{ff}$

As described, coefficients are functions of the Peclet number, which is defined as the relation between the convective and diffusive term for each face  $(F_f/D_f)$ .

If a QUICK scheme is applied, additional terms that correspond to the downstream neighbours are introduced.

$$a_{EE} = -\max\left(0, -\frac{1}{8}F_e\right) \quad (2.19)$$

$$a_{WW} = -\max\left(0, \frac{1}{8}F_w\right) \quad (2.20)$$

The  $a_p$  term is computed as a sum of all terms

$$a_P = a_E + a_W + a_{EE} + a_{WW} \quad (2.21)$$

### 2.3.4. Boundaries

The boundary conditions are used to specify the flow behavior over the surfaces that define the domain of study. Two different boundary conditions are commonly used.

Dirichlet condition is used to set the value of a variable at the boundaries. This condition is useful to set physical walls (no velocity through them), and also isothermal boundaries with a specific temperature. This condition is also used to impose a specific value of pressure at the outlet of open cavities.

Neumann condition is used to set null gradient at the boundaries. This condition is useful to impose continuity on the variable field, which means continuity on the flow, as symmetry walls. This condition is also used to set adiabatic walls. Moreover, this boundary condition is applied on the pressure field to ensure that the applied pressure over physical walls is the same as the pressure of the nearest flow volume.

## 2.4. Temporal Discretization

In this section the temporal discretization of the algorithm used to solve the low-Mach Navier-Stokes equations is exposed. The algorithm proposed by Lessani and Papalexandris [2] is based on the fractional step method with a predictor-corrector steps that can be applied to open and closed cavities. The temporal discretization applied involves three time-steps. Each time-step is identified by a subscript, where the newest one is identified with  $t_{n+1}$ , and the other ones as  $t_n$  and  $t_{n-1}$ .

The algorithm and also the temporal discretization are divided in two steps, the predictor step and the corrector step. This method reduces the effects of the density derivative on the final solution.

### 2.4.1. Predictor Step

As a first step, the predictor variables ( $t_l$ ) are evaluated.

1. Compute the predictor values for the scalar variables based on the previous stages at time  $t_{n-1}$  and  $t_n$  and applying an Adams – Bashforth scheme for the temporal discretization.

$$\rho_n \cdot \frac{\phi_l - \phi_n}{\Delta t} \cdot V_{cv} = \frac{3}{2} R(\phi_n) - \frac{1}{2} R(\phi_{n-1}) \quad (2.22)$$

2. For closed systems evaluate the thermodynamic pressure using the temperature (obtained from the enthalpy).

$$P_0 = \frac{M_0 \cdot R_g}{\int \frac{dV}{T_l}} \quad (2.23)$$

3. Compute the predictor values for the density by applying the state equation.

$$\rho_l = \frac{P_0}{R_g T_l} \quad (2.24)$$

4. Compute the pseudo – predictor velocities based on the previous stages at time  $t_{n-1}$  and  $t_n$  using the momentum equations without the dynamic pressure and applying and Adams – Bashforth scheme for the temporal discretization.

$$\frac{\rho_l u_p - \rho_n u_n}{\Delta t} \cdot V_{cv} = \frac{3}{2} R(\rho_n u_n) - \frac{1}{2} R(\rho_{n-1} u_{n-1}) \quad (2.25)$$

5. Solve the Poisson equation and get the predictor dynamic pressure. The divergence of the velocity field is computed with the derivative of the density.

$$\nabla^2 p = \left( \nabla \cdot (\rho u_p) + \frac{\partial \rho_l}{\partial t} \right) \cdot \frac{1}{\Delta t} \quad (2.26)$$

6. Compute the predictor velocities using the predictor dynamic pressure.

$$\frac{\rho_l u_l - \rho_n u_n}{\Delta t} = - \frac{\partial p_l}{\partial x_i} \quad (2.27)$$

### 2.4.2. Corrector Step

With the predictor variables, the corrector step is evaluated. As it can be seen, it is similar to the predictor step but it uses a Crank-Nicholson scheme to discretize the temporal term on the scalar transport equation.

7. Compute the corrector values for the scalar variables based on the previous stages at time  $t_l$  and  $t_n$  and applying a Crank – Nicholson scheme for the temporal discretization.

$$\rho_l \cdot \frac{\phi_{n+1} - \phi_n}{\Delta t} \cdot V_{cv} = \frac{1}{2} R(\phi_l) + \frac{1}{2} R(\phi_n) \quad (2.28)$$

8. For closed systems evaluate the thermodynamic pressure using the temperature (obtained from the enthalpy).

$$P_0 = \frac{M_0 \cdot R_g}{\int \frac{dV}{T_{n+1}}} \quad (2.29)$$

9. Compute the predictor values for the density by applying the state equation.

$$\rho_{n+1} = \frac{P_0}{R_g T_{n+1}} \quad (2.30)$$

10. Compute the pseudo – corrector velocities based on the previous stages at time  $t_l$  and  $t_n$  using the momentum equations without the dynamic pressure and applying and Adams – Bashforth scheme for the temporal discretization.

$$\frac{\rho_{n+1} u_p - \rho_n u_n}{\Delta t} \cdot V_{cv} = \frac{3}{2} R(\rho_l u_l) - \frac{1}{2} R(\rho_n u_n) \quad (2.31)$$



11. Solve the Poisson equation and get the corrector dynamic pressure. The divergence of the velocity field is computed with the derivative of the density.

$$\nabla^2 p = \left( \Delta \cdot (\rho u_p) + \frac{\partial \rho_{n+1}}{\partial t} \right) \cdot \frac{1}{\Delta t} \quad (2.32)$$

12. Compute the corrector velocities using the predictor dynamic pressure.

$$\frac{\rho_{n+1} u_{n+1} - \rho_n u_n}{\Delta t} = - \frac{\partial p_{n+1}}{\partial x_i} \quad (2.33)$$

To solve the Poisson equation that appears on both steps, a Gauss – Seidel method, also known as the Liebmann method, is used. This method is an iterative method used to solve a linear system of equations, and convergence is only ensured if the matrix is diagonal dominant, or symmetric and positive defined, which is accomplished in this case.

### 2.4.3. Stability

The algorithm presented uses a time step on each iteration. This value is extremely important on explicit algorithms, where high values may introduce numerical errors. In this study, two different conditions are used [4]. The first one is the CFL condition which imposes a relation between the time-step ( $\Delta t$ ), the grid size ( $\Delta x_i$ ) and the velocity of the flow. All of them related with the Courant number, which is set in a range from 0.1 to 0.3 in this study.

$$\Delta t = Co \cdot \min \left( \frac{\Delta x_i}{u_i} \right) \quad (2.34)$$

The main objective of this value is to ensure that each particle of the flow does not cross more than one control volume per iteration. The second condition is related with numerical stability taking into account the diffusive terms. This relation is important in zones where diffusion dominates over convection.

$$\Delta t = Co \cdot \frac{1}{2} \cdot \min \left( \frac{\Delta x_i^2}{\frac{\mu}{\rho}, \frac{\lambda}{\rho \cdot c_p}} \right) \quad (2.35)$$

The final time step is set equal to the minimum value.

## 2.5. Verification

With the aim of verifying the implementation of the low-Mach NS equations, two tests have been performed. The first one is the lid driven cavity, which is used to check the momentum and pressure equations. The second one is the heated cavity with large temperature variations and variable properties, which is used to check the scalar equation of the energy and the computation of density, thermodynamic pressure and also the flow properties. An additional test is also performed to check the parallelization of the code and its scalability.

### 2.5.1. Test – Driven Cavity

The driven cavity test consists on studying an incompressible flow in a square cavity with a slip velocity applied on one wall. Results are compared with benchmark solutions [8].

The problem is defined by three static walls and one dynamic wall. For the static walls a Dirichlet condition is used to set a non-slip condition. The top wall is the dynamic one and has a slip velocity, which introduces the movement into the cavity.

Due to the three dimensional capabilities of the code implemented, front and back walls have a Neumann condition for all variables. This leads to a 2D problem without the effects of the enclosure on the third dimension.

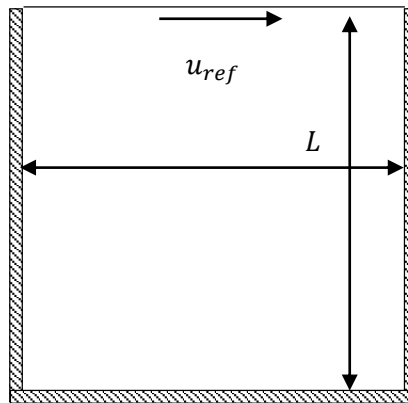


**Figure 3.** Geometry and boundary conditions for the lid driven cavity problem.

To close the problem the Reynolds number must be defined.

$$Re = \frac{\rho u_{ref} L}{\mu} \quad (2.36)$$

This is useful to identify the behavior of different flows, taking in account its properties and also geometry and velocity. For each Reynolds number, a specific set of reference solutions can be found in the literature. In this case, the reference velocity is computed from the desired Reynolds and imposed as a boundary condition on the top wall. There are reference solutions from a wide range of Reynolds, but on this section only results for a  $Re = 3200$  computed with a  $128 \times 128$  mesh and SP scheme are shown. Velocity profiles on the middle of the cavity and also stream lines are compared with the reference in **Figure 4** and **Figure 5**. Both comparisons show an agreement between the numerical results and the reference ones.

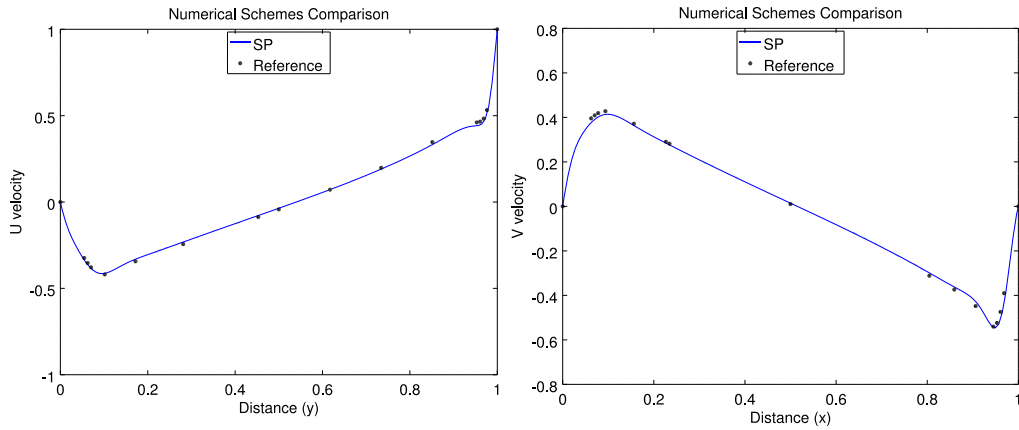


**Figure 4.** Vertical  $v_x$  profile at  $x = 0.5$  (left) and horizontal  $v_y$  profile at  $y = 0.5$  (right) for the lid driven cavity at  $Re = 3200$  using a  $128 \times 128$  control volumes (CV) mesh.

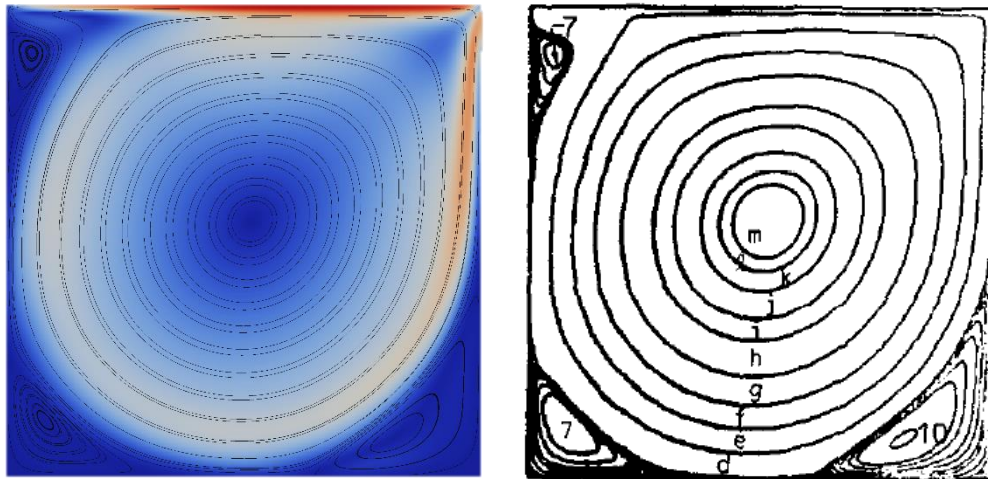


**Figure 5.** Velocity field of the lid driven cavity at  $Re = 3200$  using a  $128 \times 128$  CV mesh (left) and reference stream lines from Ghia et. al. [8] (right).

These results are also useful to verify that implementation of momentum and pressure equations are correct and no undesired behaviors occur during its computation.

### 2.5.2. Test – Heated Cavity

The heated cavity test consists on studying a variable density flow in a differentially heated square cavity with a large temperature difference between its vertical walls. Results are compared with the benchmark solutions from Vierendeels, Merci and Dick [9].

The case is defined by two isothermal walls, each one at  $T_h$  and  $T_c$ , respectively, and two adiabatic walls, with gravity parallel to the isothermal walls.

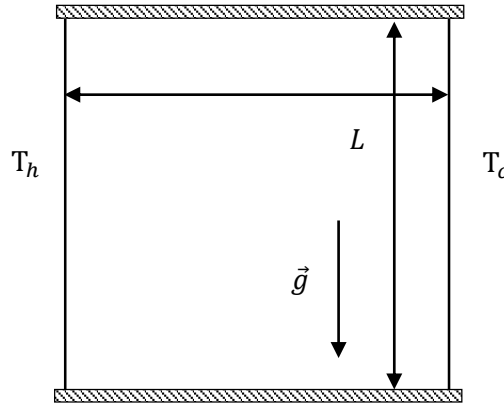


**Figure 6.** Geometry and boundary conditions for the heated cavity problem.

To close the problem, a set of dimensionless groups are defined:

- Prandtl number: This number compares the momentum and heat transport. In this case, Prandtl number is set constant and equal to 0.71.
- Temperature difference: Temperatures are defined through the  $\varepsilon$  parameter.

$$\varepsilon = \frac{T_h - T_c}{2T_0} \quad (2.37)$$

- Fluid properties: Viscosity and conductivity are computed with the following expressions.

$$\mu(T) = \mu_{ref} \cdot \left( \frac{T}{T_{ref}} \right)^{\frac{3}{2}} \cdot \frac{T_{ref} + 110.5}{T + 110.5} \quad (2.38)$$

Where  $T_{ref} = 273 \text{ K}$  and  $\mu_{ref} = 1.68 \cdot 10^{-5} \text{ Kg}/(\text{m} \cdot \text{s})$ .

- Rayleigh number: It expresses the relation between the natural convection and diffusivity.

$$Ra = Pr \cdot \frac{g\rho_0^2(T_h - T_c)L^3}{T_0\mu_0^2} \quad (2.39)$$

Where  $T_0 = 600\text{ K}$ , at which fluid properties are evaluated. For each Rayleigh number there is a unique gravity value that satisfies this equation.

Benchmark solutions are presented in a dimensionless form, using  $T_0$  and a reference velocity  $v_{ref}$ . This velocity is computed using the Boussinesq solution for the natural convective heat transfer problem.

$$v_{ref} = Ra^{0.5} \frac{\mu(T_0)}{\rho_0 L} \quad (2.40)$$

On this section results for a  $Ra = 10^6$  and  $\varepsilon = 0.6$  computed using a  $128 \times 128$  CV mesh and different numerical schemes are exposed. Velocity and temperature profiles on the middle of the cavity and also stream lines and temperature contours are compared with the reference ones in **Figure 7**, **Figure 8** and **Figure 9**.

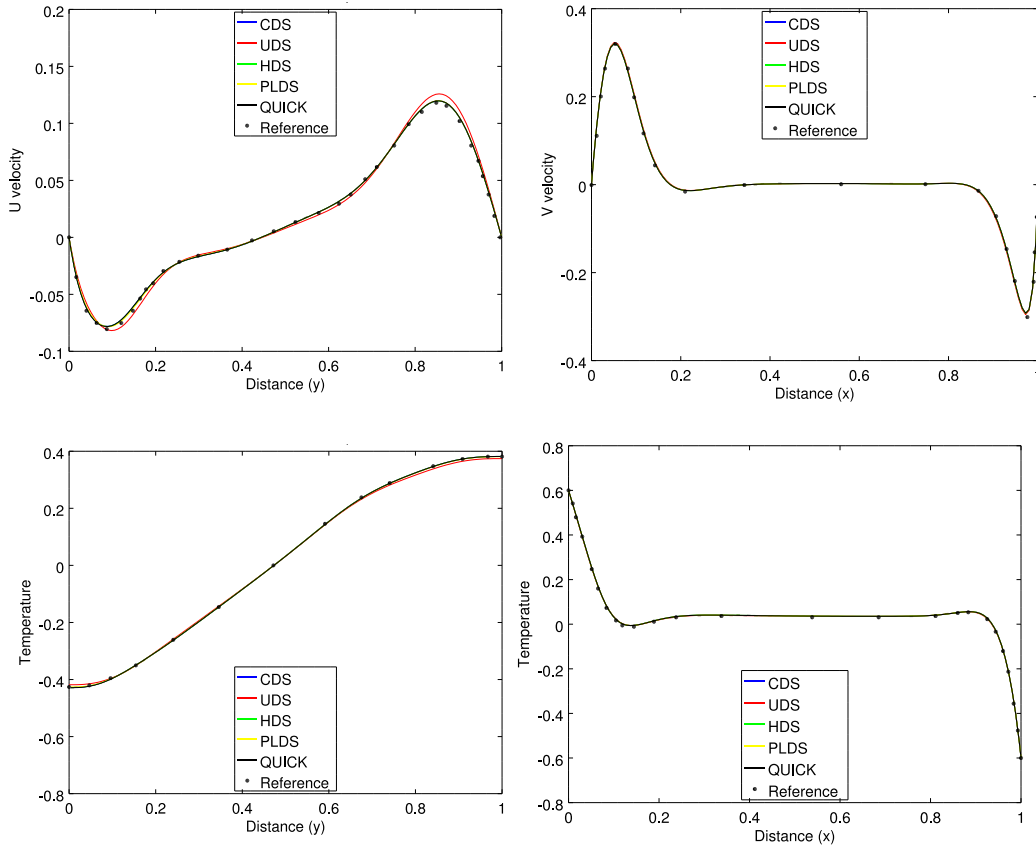


**Figure 7.** Vertical  $u$  profile at  $x = 0.5$  (top – left), horizontal  $v$  profile at  $y = 0.5$  (top – right), temperature profile at  $x = 0.5$  (bottom – left) and temperature profile at  $y = 0.5$  (bottom – right) using a  $128 \times 128$  CV mesh.

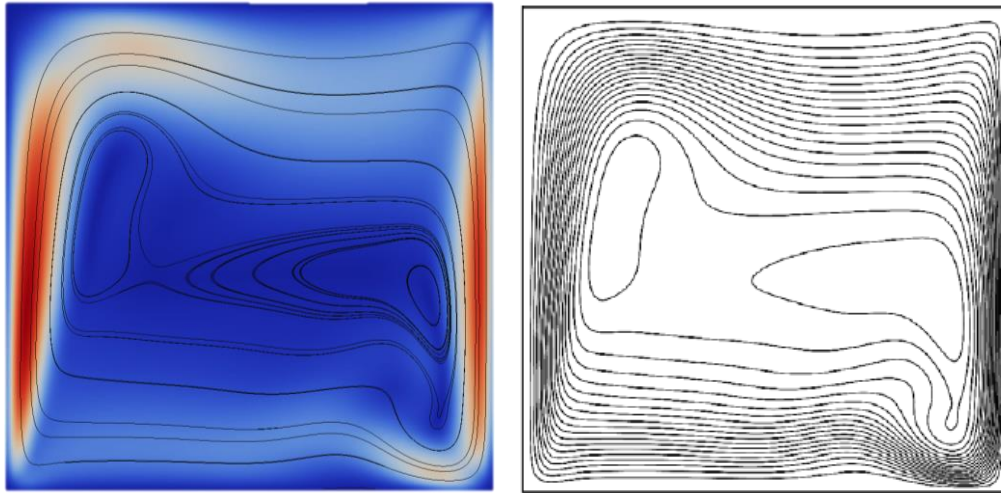


**Figure 8.** Velocity field of the heat cavity at  $Ra = 10^6$  using a  $128 \times 128$  CV mesh (left) and reference stream lines from Vierendeels et. al. [9] (right).

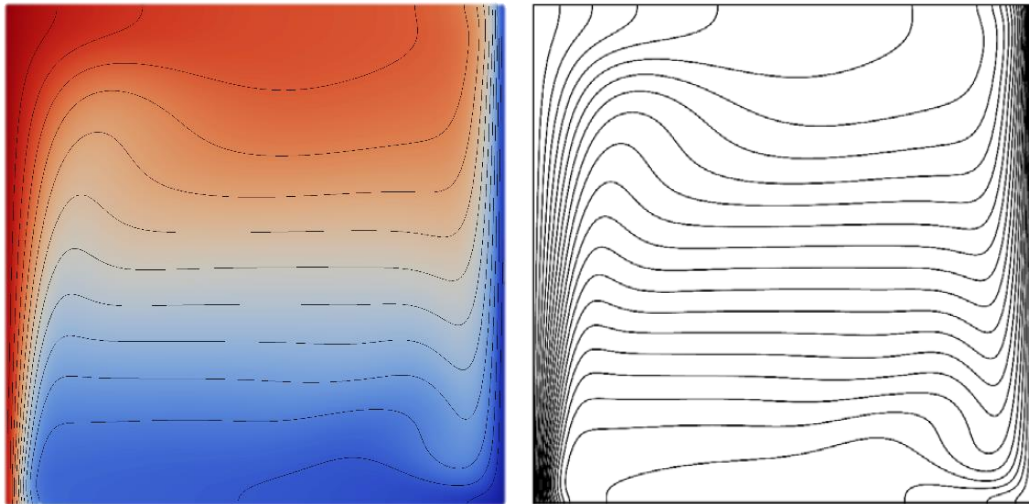


**Figure 9.** Temperature field of the heat cavity at  $Ra = 10^6$  and  $128 \times 128$  mesh (left) and reference contours from Vierendeels et. al. [9] (right).

Other parameters of interest are the thermodynamic pressure of the cavity and the Nusselt evaluated at the isothermal walls.

**Table 2.** Comparison of Nusselt numbers and thermodynamic pressure of different schemes and reference values.

<b>Variables</b>	<b>CDS</b>	<b>UDS</b>	<b>HDS</b>	<b>PLDS</b>	<b>QUICK</b>	<b>Vierendeels et .al. [9]</b>
$Nu_{max-Right}$	18.093	18.425	18.094	18.101	18.115	15.519
$Nu_{min-Right}$	0.735	1.057	0.739	0.787	0.712	0.758
$Nu_{Right}$	9.394	9.523	9.393	9.395	9.395	8.637
$Nu_{max-Left}$	20.492	20.699	20.485	20.464	20.505	20.270
$Nu_{min-Left}$	1.054	1.170	1.054	1.062	1.052	1.067

<i>Variables</i>	<i>CDS</i>	<i>UDS</i>	<i>HDS</i>	<i>PLDS</i>	<i>QUICK</i>	<i>Vierendeels et .al. [9]</i>
$\overline{Nu}_{Left}$	8.655	8.769	8.654	8.656	8.653	8.687
$P/P_0$	0.9244	0.9269	0.9244	0.9248	0.9242	0.9245

Results show that the low-Mach equations are giving accurate results for compressible flows at low Mach numbers. This also means that implementation of the scalar equation of energy and the computation of the flow properties are correct. As it can be seen on the Nusselt values in **Table 2**, the cold wall (right) tends to show higher values than the expected ones. This, in fact, could be related with the scale of the boundary layer, which on the cold wall is smaller than the hot wall. Even so, all numerical schemes implemented give accurate results on the velocity computation.

### 2.5.3. Test – Parallel Execution

With the objective of reducing the computational time required to solve the algorithm, the developed code is parallelized to be able to use more than a unique thread. This means that part of the code can be run in a parallel way. It is important to note that this could introduce a new kind of error, such as memory overlapping that needs to be checked. Moreover it is also interesting to check the scalability of the program as more threads are added to the simulation.

For this case, the last test of the heated cavity is executed for a different number of threads. Then, results and computation times are compared. Due to hardware limitations, tests are carried on a quad core hyper threading CPU with 4 physical cores.

All cases show accurate results which means that no errors due to parallel programming appears during the execution. Moreover, the execution times for different number of cores show the scalability of the code.

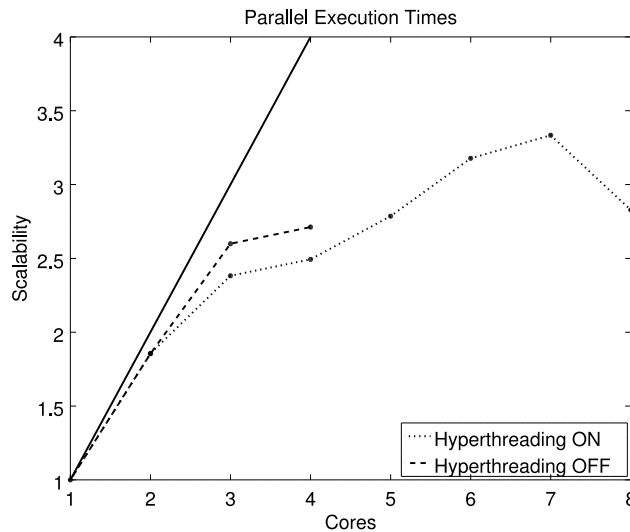


**Figure 10.** Computational scalability and number of threads (Heated cavity at  $Ra = 10^6$  and  $\varepsilon = 0.6$  using a  $128 \times 128$  CV mesh).

Results show that the best performance is achieved for 7 threads, so further analysis will be done with this configuration. As expected, the scalability is more or less linear until the third thread. For more threads, the scalability becomes not linear, but an important speedup is achieved with the hyper threading technology. Moreover, for 8 threads configuration the computational time increases. This could be related with the operations required by the operating system (OS), which may increase the computational time of one core. Thus, the overall time of the simulation increases due to synchronization barriers.



## 3. Reacting Flows

### 3.1. Introduction

Nowadays, many industrial devices use reacting flows as a source of energy, as combustion engines, which take profit of the chemical energy of reactants to produce mechanical work. In all cases the challenge is to improve its efficiency, which means use less fuel to obtain more power or heat. These processes involve complex chemical reactions and high gradients of temperatures, which increases the difficulty to improve them. CFD codes with reacting flows could be highly used with the aim of simulating the physics of combustion processes and ease the development of novel designs with better efficiencies.

In general, solving combustion processes with CFD codes means to study the behavior of the flow, but also chemical reactions and species transport through the domain at the same time. Complex chemical mechanisms may introduce thousands of species and thousands of reactions, which added to the fact that combustion processes usually imply smaller scales than the flow ones, the computational requirements increase rapidly.

This chapter focuses on the species transport equations at low Mach numbers, taking into account multiple chemical reactions and variable properties of each species. At the end different tests used to verify the developed code are exposed.

### 3.2. Species Characterization

Before the introduction of the species transport equation and its coupling with the low – Mach algorithm, the species characterization is presented.

#### 3.2.1. Thermochemistry

Species are identified by its mass fraction  $Y_k$ , for  $k = 1$  to  $N$  where  $N$  is the total number of species. The mass fraction is computed with the mass of the  $k_{th}$  species ( $m_k$ ) and the total mass ( $m$ ).

$$Y_k = \frac{m_k}{m} \quad (3.1)$$

The species transport equation uses the mass fractions as the scalar field on the convective-diffusive equation. This means that reacting flows need  $N$  more equations to solve per iteration.

Species have different properties. Hence, thermodynamic properties of a multi-species gas needs to be computed. The mixture density and the thermodynamic pressure can be expressed as a sum of the species density and partial pressure respectively [10].

$$\rho = \sum_{k=1}^N \rho_k \quad (3.2)$$

$$P = \sum_{k=1}^N p_k = \sum_{k=1}^N \rho_k \frac{R}{W_k} T = \rho \frac{R}{W} T \quad (3.3)$$

where  $W$  is the mean molecular mass of the mixture.

$$\frac{1}{W} = \sum_{k=1}^N \frac{Y_k}{W_k} \quad (3.4)$$

Heat capacity is computed as a function of temperature, while the mixture heat capacity is obtained from the species heat capacity and mass fractions.

$$c_p = \sum_{k=1}^N c_{p,k}(T) \cdot Y_k \quad (3.5)$$

### 3.2.2. Chemical Kinetics

The combustion process involves many chemical reactions. All these reactions must be used to compute the rates of production for each species. Applying the mass conservation for each reaction, the following equation can be obtained.

$$\sum_{k=1}^N v'_{kj} \cdot W_k = \sum_{k=1}^N v''_{kj} \cdot W_k \quad (3.6)$$

Where  $v'_{kj}$  and  $v''_{kj}$  represents the stoichiometric coefficients of species  $k$  in reaction  $j$ . Coefficients of equation ( 3.6 ) can be simplified using a global coefficient  $v_{kj}$ , computed as  $v_{kj} = v''_{kj} - v'_{kj}$ .

$$\sum_{k=1}^N v_{kj} \cdot W_k = 0 \quad (3.7)$$

Each reaction has an inherent velocity of reaction, which is directly related with the rate of production of each species. Taking into account the equation of chemical kinetics, the reaction velocity is given by the product of the molar concentrations with the reaction constants. This leads to the equation for the rate of progress  $Q$  of reaction  $j$  [10].

$$Q_j = K_{fj} \prod_{k=1}^N \left( \frac{\rho Y_k}{W_k} \right)^{v'_{kj}} - K_{rj} \prod_{k=1}^N \left( \frac{\rho Y_k}{W_k} \right)^{v''_{kj}} \quad (3.8)$$

The reaction constants  $K_{fj}$  and  $K_{rj}$  are the forward and reverse constants, which are usually modeled with the Arrhenius law.

$$K_{fj} = A_j T^{\beta_j} \cdot \exp\left(-\frac{Ea_j}{RT}\right) \quad (3.9)$$

$$K_{rj} = \frac{K_{fj}}{\left(\frac{P_0}{RT}\right)^{\sum_{k=1}^N v_{kj}} \cdot \exp\left(\frac{\Delta S_j^0}{R} - \frac{\Delta H_j^0}{RT}\right)} \quad (3.10)$$

For each reaction, coefficients  $A_j$  (pre-exponential constant),  $\beta_j$  (temperature exponent) and  $Ea_j$  (activation energy) must be known. The  $\Delta S_j^0$  and  $\Delta H_j^0$  are the entropy and enthalpy changes for reaction  $j$  respectively.

Finally, the rate of progress of each reaction is used to compute the rate of production for each species from all reactions involved.

$$\dot{\omega}_k = \sum_{j=1}^M \dot{\omega}_{kj} = W_k \cdot \sum_{j=1}^M \nu_{kj} Q_j \quad (3.11)$$

Rates of progress could need space and time scales smaller than non-reacting flows, which implies higher computational times as detailed by Poinso and Veynante [10].

As it can be seen on equation ( 3.8 ), the exponents of the concentrations are set to the stoichiometric coefficients. This is only true if complex reaction schemes are used, where each reaction corresponds to an elementary reaction. There are alternative mechanisms with specific coefficients that only use a fraction of the total reactions and species. These ones are interesting to reduce the computational requirements.

### 3.2.1. Thermodynamic Properties

As explained before, each species has specific properties that depends on temperature. These properties are modeled with the following correlations.

$$c_p(T) = R(a_0 + a_1T + a_2T^2 + a_3T^3 + a_4T^4) \left( \frac{J}{molK} \right) \quad (3.12)$$

$$h(T) = RT \left( a_0 + \frac{a_1}{2}T + \frac{a_2}{3}T^2 + \frac{a_3}{4}T^3 + \frac{a_4}{5}T^4 + \frac{a_5}{T} \right) \left( \frac{J}{mol} \right) \quad (3.13)$$

$$s(T) = a_0 \ln(T) + a_1T + \frac{a_2}{2}T^2 + \frac{a_3}{3}T^3 + \frac{a_4}{4}T^4 + a_6 \quad (3.14)$$

$$\mu = e^{b_0 + b_1 \ln T + b_2 (\ln T)^2 + b_3 (\ln T)^3} \left( \frac{Kg}{ms} \right) \quad (3.15)$$

$$\lambda = e^{c_0 + c_1 \ln T + c_2 (\ln T)^2 + c_3 (\ln T)^3} \left( \frac{W}{mK} \right) \quad (3.16)$$

It is interesting to note that enthalpy includes sensible and formation enthalpy. Polynomic coefficients of each species are obtained from the NASA technical memorandum [11] (thermodynamic properties) and from CHEMKIN (transport properties). Coefficients are specified on the Appendix A.

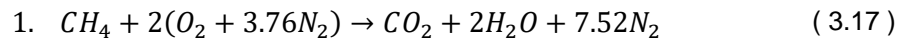
### 3.3. Chemical Models

All combustion processes are complex phenomena that involve multiple chemical reactions with complex kinetics. Chemical mechanisms involving thousands of species and thousands of reactions are commonly used with the aim of obtaining accurate results in the evolution of temperature and species. Therefore it seems natural to use these models. But as seen on the last section, complex reactions and multiple species requires solving a transport equation for each species, taking into account the effect of all reactions on it. Hence, when dealing with complex geometries and also fine meshes it requires more computational resources and also more computational time. This often is against the demands of industry, which expects rapidity and also accurate results.

For this reason simplified models are often used, where only some species are introduced with the appropriate reactions. In this project, two different models have been used, the first one composed by a unique and irreversible reaction, and the second one composed by four reactions.

#### 3.3.1. Single Step CH<sub>4</sub> / Air Model

The first chemical model presented is a single step CH<sub>4</sub> / Air combustion.



Taking into account the air composition, the stoichiometric mass fractions are specified in **Table 3**.

**Table 3.** Mass fractions for reactants at stoichiometric conditions.

<i>Species</i>	<i>Mass Fraction</i>
$\text{CH}_4$	0.055
$\text{O}_2$	0.220
$\text{N}_2$	0.725

For the products, the stoichiometric fractions are specified in **Table 4**.

**Table 4.** Mass fractions for products at stoichiometric conditions.

<i>Species</i>	<i>Mass Fraction</i>
$\text{CO}_2$	0.151
$\text{H}_2\text{O}$	0.124
$\text{N}_2$	0.725

Due the simplicity of the model, a lumped model for chemical kinematics is used with the objective to obtain more accurate results.

**Table 5.** Coefficients applied on the Arrhenius equation.

<b>Reaction</b>	<b><math>A \left( \frac{\text{mole}}{\text{cm}^3 \cdot \text{s}} \right)</math></b>	<b><math>\beta</math></b>	<b><math>Ea/R \text{ (K)}</math></b>
1	$3.97121839094 \cdot 10^{28}$	0.0	16900

**Table 6.** Coefficients applied on the rate of progress computation.

<b>Reaction</b>	<b><math>CH_4</math></b>	<b><math>O_2</math></b>	<b><math>CO_2</math></b>	<b><math>H_2O</math></b>
1	2.8	1.2	0.0	0.0

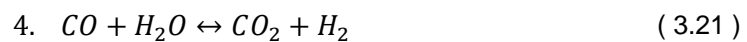
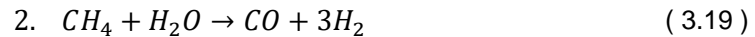
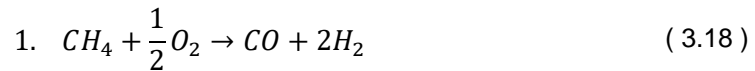
Other parameters of interest are the molar masses. Due to its implication with large numbers, a high accuracy must be provided to it with the objective to ensure mass conservation on each chemical reaction.

**Table 7.** Molar mass of species involved on the simple step mechanism.

<b>Species</b>	<b>Molar Mass (kg/mol)</b>
$CH_4$	$0.1604303026 \cdot 10^{-1}$
$O_2$	$0.3199880028 \cdot 10^{-1}$
$CO_2$	$0.4400995064 \cdot 10^{-1}$
$H_2O$	$0.1801534009 \cdot 10^{-1}$
$N_2$	$0.2801339912 \cdot 10^{-1}$

### 3.3.2. Four Step CH<sub>4</sub> / Air Model

A multiple step model is also used. This model was proposed by Jones and Lindstedt [12] and uses a four reactions mechanism for methane combustion.



As on the single step mechanism, a lumped model for chemical kinematics is used with the objective to obtain more accurate results.

**Table 8.** Coefficients applied on the Arrhenius equation.

<i>Reaction</i>	$A \left( \frac{\text{mole}}{\text{cm}^3 \cdot \text{s}} \right)$	$\beta$	$Ea/R \text{ (K)}$
1	$7.82442940417126 \cdot 10^{13}$	0.0	15096.5
2	$0.300 \cdot 10^{12}$	0.0	15096.5
3	$4.44569852509731 \cdot 10^{18}$	-1.0	20128.7
4	$0.275 \cdot 10^{13}$	0.0	10064.3

**Table 9.** Coefficients applied on the rate of progress computation.

<i>Reaction</i>	$CH_4$	$O_2$	$CO$	$CO_2$	$H_2O$	$H_2$
1	0.5	1.25	0	0	0	0
2	1	0	0	0	1	0
3	0	2.25	0	0	-1.0	0.5
4	0	0	1	0	1	0

The equilibrium reaction of water must include the backward coefficients.

**Table 10.** Coefficients applied on the backward rate of progress computation.

<i>Reaction</i>	$CH_4$	$O_2$	$CO$	$CO_2$	$H_2O$	$H_2$
3	0	1.75	0	0	0	-0.5
4	0	0	0	1	1	0

Molar mass of the species added on this chemical mechanism are the following.

**Table 11.** Molar mass of added species on the four step mechanism.

<i>Species</i>	<i>Molar Mass (kg/mol)</i>
$CO$	$0.2801055050 \cdot 10^{-1}$
$H_2$	$0.2015939951 \cdot 10^{-2}$

### 3.4. Governing Equations

#### 3.4.1. Species Conservation

The governing equations for variable density reacting flows are derived from the conservation of mass equation.

$$\frac{\partial \rho Y_k}{\partial t} + \frac{\partial}{\partial x_i} (\rho (u_i + V_{k,i}) Y_k) = \dot{\omega}_k \quad (3.22)$$

These equations introduce the rate of progress of each reaction. In the equation appears a  $V_{k,i}$  velocity, which introduces the molecular diffusion into the mass conservation [10]. By definition, the overall rate of progress and also molecular diffusivities must be zero.

$$\sum_{k=1}^N Y_k \cdot V_{k,i} = 0 \quad (3.23)$$

$$\sum_{k=1}^N \dot{\omega}_k = 0 \quad (3.24)$$

The computation of the molecular diffusive velocities is a problem itself, which involves a system of equations of size  $N^2$ . Usually simplifications based on Fick's law are used to compute these velocities and focus all the efforts to solve the combustion.

$$V_{k,i} \cdot Y_k = -D_k \frac{\partial Y_k}{\partial x_i} \quad (3.25)$$

where  $D_k$  is the diffusion coefficient of the species  $k$  into the mixture. This can be computed from the Lewis number, which is defined as the relation between the thermal diffusion coefficient ( $D_{th}$ ) and the molecular diffusion coefficient. Lewis number is more or less constant and known for many species in many flames [10].

$$Le_k = \frac{\lambda}{\rho c_p D_k} = \frac{D_{th}}{D_k} \quad (3.26)$$

**Table 12.** Lewis number for different species used on computations.

	$C_3H_8$	$CH_4$	$O_2$	$CO$	$CO_2$	$H_2O$	$H_2$	$N_2$
$Le_k$	1.84	0.97	1.11	1.39	1.39	0.83	1	1



Applying Fick's law the species equation becomes.

$$\frac{\partial \rho Y_k}{\partial t} + \frac{\partial}{\partial x_i} (\rho Y_k u_i) = \frac{\partial}{\partial x_i} \left( \rho D_k \frac{\partial Y_k}{\partial x_i} \right) + \dot{\omega}_k \quad (3.27)$$

Due to the simplification of the molecular diffusivities, equation ( 3.23 ) is not satisfied and the application of this methodology could lead to important errors on the computation of mass fractions. To ensure mass conservation, the last species is computed with the other mass fractions to ensure that the sum of all mass fractions is equal to 1. This method is only applicable if the concentration of the last species is higher than the others (acts as a diluent), and not plays an important role on the combustion process. The best candidate that accomplishes these specifications in air flames is nitrogen.

There is an alternative method that uses a correction velocity to ensure mass conservation, but it increases the difficulty of its implementation and also the computational time required.

Finally, the final species transport equation is obtained in its non-conservative.

$$\rho \frac{\partial Y_k}{\partial t} = -\rho u_i \frac{\partial}{\partial x_i} (Y_k) + \frac{\partial}{\partial x_i} \left( \rho D_k \frac{\partial Y_k}{\partial x_i} \right) + \dot{\omega}_k \quad (3.28)$$

### 3.4.2. Energy Conservation

The definition of the energy conservation equation is crucial to define properly the combustion process. As many species are involved in a combustion process, the energy conservation equation is modified by considering both sensible enthalpy and formation enthalpy.

$$h = \sum_{k=1}^N Y_k \cdot \left( \Delta h_{f,k}^0 + \int_{T_0}^T c_{p,k} dT \right) \quad (3.29)$$

The new enthalpy transport equation is similar to the one used on the low-Mach equations, but a term for the molecular diffusivity is added.

$$\rho \frac{\partial h}{\partial t} = -\rho u_i \frac{\partial h}{\partial x_i} + \frac{dP_0}{dt} - \frac{\partial \dot{q}_i}{\partial x_i} \quad (3.30)$$

where

$$\dot{q}_j = -\lambda \frac{\partial T}{\partial x_i} - \rho \sum_{k=1}^N h_k D_k \frac{\partial Y_k}{\partial x_i} \quad (3.31)$$

This term corresponds to Fourier's law of conduction plus the enthalpy transport due to molecular diffusion. To recover the temperature, a non-linear system of equations must be solved (i.e. Newton-Raphson). The drawback is that it increases the computational time. With the aim of reducing it, it becomes more useful to compute directly the temperature with its transport equation.

$$\rho c_p \frac{\partial T}{\partial t} = -\rho c_p u_i \frac{\partial T}{\partial x_i} + \frac{\partial}{\partial x_i} \left( \lambda \frac{\partial T}{\partial x_i} \right) + \left( \rho \sum_{k=1}^N c_{p,k} Y_k V_{k,i} \right) \frac{\partial T}{\partial x_i} + \dot{\omega}_T \quad (3.32)$$

The new term on the right hand side  $\dot{\omega}_T$  corresponds to the combustion heat release due to the formation and sensible enthalpy variations. This heat release is not the same defined on the chemistry section, but is related.

$$\dot{\omega}_T = - \sum_{k=1}^N h_k \dot{\omega}_k \quad (3.33)$$

As mentioned by Poinso and Veynante [10], molecular diffusion in the energy equation may be neglected, which is a common procedure in many codes due to its difficulty to be implemented and computed.

The final equation used to compute the temperature is the following one.

$$\rho c_p \frac{\partial T}{\partial t} = -\rho c_p u_i \frac{\partial T}{\partial x_i} + \frac{\partial}{\partial x_i} \left( \lambda \frac{\partial T}{\partial x_i} \right) + \dot{\omega}_T \quad (3.34)$$

#### 3.4.3. Radiation

Behavior of flames is clearly affected by the radiation emitted, absorbed and dissipated. This energy transport has a direct influence on the laminar speed flame, stability of the front flame and also flammability and extinction.

Radiation effects may be introduced by using the radiative transfer equation.

$$\frac{dI_{\lambda\omega}}{ds} = \kappa_{\lambda} I_{b,\lambda\omega} + \frac{\sigma_{s,\lambda}}{4\pi} \int_{4\pi} I_{\lambda\omega} \Phi_{\vec{s}' \rightarrow \vec{s}} d\omega' - \kappa_{\lambda} I_{\lambda\omega} - \sigma_{s,\lambda} I_{\lambda\omega} \quad (3.35)$$

Where  $I_{\lambda\omega}$  corresponds to the Planck's radiation function,  $\kappa_{\lambda}$  to the absorption coefficient,  $\sigma_{s,\lambda}$  to the scattering coefficient and  $\Phi_{\vec{s}' \rightarrow \vec{s}}$  the probability function that represents the fraction of radiation energy on the  $\vec{s}'$  direction that is diffused over  $\vec{s}$ .

The first term of the equation describes the variation of the specific radiation intensity in the  $\vec{s}$  direction through a small volume with length  $ds$ , the second one belongs to the emitted energy of this volume in the  $\vec{s}$  direction and wave length  $\lambda$ . The third term introduces the energy diffused from other directions to  $\vec{s}$ . The fourth term represents the energy absorbed by the volume and the last one the diffused energy from  $\vec{s}$  to other directions.

When the specific radiative intensity is obtained for the overall domain, then its contribution to the energy equation can be computed.

$$-\nabla \cdot \vec{q}^R = \int_{(\lambda=0)}^{\infty} \int_{\omega=4\pi} \kappa_{\lambda} (I_{\lambda\omega} - I_{b,\lambda\omega}) d\omega d\lambda \quad (3.36)$$

Due to its difficulty, some alternative models can be found in the literature to introduce the effects of radiation. One of them is the Optically Thin Model (OTM) [13]. This model considers that the flame exchanges energy by radiation with the surrounding gas. In this way, a new expression for the radiation energy is obtained.

$$\nabla \cdot \vec{q}^R = 4\sigma(\kappa_p T_p^4 - \kappa_l T_s^4) \quad (3.37)$$

Where  $T_p$  corresponds to the temperature of volume,  $T_s$  is the temperature of the outer flow,  $\kappa_p$  the mean absorption coefficient and  $\kappa_l$  is the mean incidence coefficient. Both coefficients can be computed as a linear correlation on mixture gas with partial pressures.

Even so, the implementation of the radiation effects is not included on the scope of the project, so its implementation is left for further studies.

### 3.5. Temporal Discretization

The algorithm and temporal discretization is the same used as on the low – Mach equations. The main differences are the introduction of the chemical kinetics, the modification of the enthalpy equation by the temperature equation and the introduction of the species transport equation. In combustion processes the domain is commonly open, so thermodynamic pressure is set to a constant value (atmospheric pressure).

As in other case, the algorithm is divided in two steps. In this section only the previous calculations of each step related with combustion are described.

#### 3.5.1. Predictor Step

As a first step, the predictor variables are calculated.

1. Compute the rates of progress of each reaction and also the rates of production for each species at each control volume using  $t_n$  variables on equations ( 3.11 ) and ( 3.13 ).
2. Compute the predictor values for the scalar variables (temperature and species) based on the previous stages at time  $t_{n-1}$  and  $t_n$  and applying an Adams – Bashforth scheme for the temporal discretization.

$$\rho_n \cdot \frac{\phi_l - \phi_n}{\Delta t} \cdot V_{cv} = \frac{3}{2} R(\phi_n) - \frac{1}{2} R(\phi_{n-1}) \quad (3.38)$$

#### 3.5.2. Corrector Step

With the predictor variables, the corrector step is computed. As it can be seen, it is similar to the predictor step but it uses a Crank-Nicholson scheme to discretize the temporal integration on the scalar transport equation.

1. Compute the rates of progress of each reaction and also the rates of production for each species at each control volume using  $t_l$  variables on equations ( 3.11 ) and ( 3.13 ).
2. Compute the corrector values for the scalar variables (temperature and species) based on the previous stages at time  $t_l$  and  $t_n$  and applying a Crank – Nicholson scheme for the temporal discretization.

$$\rho_l \cdot \frac{\phi_{n+1} - \phi_n}{\Delta t} \cdot V_{cv} = \frac{1}{2} R(\phi_l) + \frac{1}{2} R(\phi_n) \quad (3.39)$$

#### 3.5.3. Stability

The stability conditions applied on the previous algorithm are used again, but a new condition is imposed. As explained before, the production or destruction of each species depends on the rate of production and also on the time step. This is important because large time steps may produce instabilities due to high production or destructions rates. With the aim of avoiding this issue, time step is restricted to allow variations lower than 30 percent of the lowest mass fraction.

$$\Delta t = 0.30 \cdot \min \left( \frac{\rho \cdot Y_k}{\dot{\omega}_k} \right) \quad (3.40)$$

To avoid small time steps due to null mass fractions, a minimum value of  $10^{-6}$  is imposed.

### 3.6. Laminar Flames

Computation of laminar flames is a first step toward more complex configurations. These cases can be easily compared with theoretical approaches and experimental results. These are useful to validate chemical mechanisms and their implementation. There are two canonical flame configurations, which differs in the fuel and oxidizer injection.

#### 3.6.1. Premixed Flames

Premixed flames are characterized by a unique fuel and oxidizer inlet. Combustion takes place in a thin reaction with high rates of production. These kind of flames are characterized by a total combustion of fuel, which increases the total energy released.

For stoichiometric and lean mixtures, fuel is not found downstream the flame, so the reduced fuel mass fraction is useful to track the combustion along the combustion chamber.

$$Y_{reduced} = \frac{Y_{fuel}}{Y_{fuel}^0} \quad (3.41)$$

As seen, it is computed taking into account the initial fuel mass fraction at the inlet and the fuel mass fraction on a specific location. This value is equal to 1 at the inlet and equal to 0 downstream the flame front. Even so, there are other methods to track the combustion process, such as the reduced temperature. This one is obtained from the maximum and minimum temperature of the flow. As seen, it goes from 0 in the fresh gases to 1 in the burnt gases.

$$\theta = \frac{T - T_{min}}{T_{max} - T_{min}} \quad (3.42)$$

Premixed flames are characterized by a flame speed. As explained, this type of flames have a common inlet of fuel and oxidizer. This allows the flame to propagate through the inlet. To understand the definition of the flame speed and its relation with the chemical kinetics, a 1D premixed flame case is developed. As a first step, the mass conservation equation taken in its steady form is applied on a control volume with a fresh gases inlet and a burnt gases outlet, identified by 1 and 2 respectively.

$$\rho_1 u_1 = \rho_2 u_2 = cte \quad (3.43)$$

If the species transport equation is also taken in its steady form, one can obtain a relation between the mass conservation equation and the rate of production, which depends on the chemical mechanism [10].

$$\rho_1 u_1 \cdot \frac{dY_k}{dx} = \frac{d}{dx} \left( \rho D \frac{dY_k}{dx} \right) + \dot{\omega}_k \quad (3.44)$$

Molecular diffusivities are null at boundaries due to homogeneous gases (no species gradient). Integration over the domain for the fuel species gives the following equation.

$$\rho_1 u_1 \cdot (Y_{fuel_2} - Y_{fuel_1}) = \int_1^2 \dot{\omega}_{fuel} dx \quad (3.45)$$

At this point, is interesting to introduce that the rate of production  $\dot{\omega}_{fuel}$  is negative and the null presence of fuel at the outlet (stoichiometric conditions).

$$\rho_1 u_1 Y_{fuel_1} = -\dot{\omega}_{fuel} \cdot \Delta x \quad (3.46)$$

The steady state is achieved when the mass flow that enters into the domain is the same as the consumption speed inside the domain. The flame speed is defined, at this point, as the velocity evaluated in the fresh gases.

$$\rho_1 S_L = \rho_1 u_1 \quad (3.47)$$

Due to the relation between the flame speed and the chemical kinetics, suitable inlet flow velocities are used to stabilize the flame front and avoid propagation effects through the inlet for each chemical mechanisms.

It is interesting to introduce the flame thickness. A correct estimation of this value before computations is an important requirement to define the grid size. A first approximation to the flame thickness is the diffusive thickness  $\delta$ . This one is obtained from an analytical solution of a simplified reaction rate expression on a unidimensional case with constant conductivities [10].

$$\delta = \frac{\lambda_{inlet}}{(\rho c_p)_{inlet} S_L} = \frac{D_{inlet}}{S_L} \quad (3.48)$$

Usually this value is quite small, and there exist correlations with better performance. One of them is the Blint correlation that proposes the following evaluation (using the Sutherland law for conductivity [10]).

$$\delta_L^b = 2\delta \cdot \left(\frac{T_2}{T_1}\right)^{0.7} \quad (3.49)$$

where  $T_2$  and  $T_1$  are the maximum and minimum temperature of the gases respectively. This one offers a more realistic value and will be used to define the minimum grid size requirements.

### 3.6.2. Non Premixed Flames

Non – premixed flames differ from the premixed ones on the composition of the inlet gas. In this case, fuel and oxidizer are introduced into the combustion chamber through different inlets. For combustion to take place, reactants must be transported and diffused into the flame zone fast enough to keep the reaction active. Usually, the flame front appears on the zone where stoichiometric conditions are reached (maximum heat release).

As expected in these cases, flames cannot propagate through the inlet (the oxidizer flow is too lean and the fuel flow is too rich), additionally, a flame speed cannot be defined. This characteristic increases the dependence of the flame front with the velocity field, which could lead to instabilities in turbulent conditions. Moreover, the thickness and location of the flame front is not constant which increases the difficulty to select a suitable size.

A mixture fraction is defined to characterize the local fuel/oxidizer ratio.

$$Z = \frac{\nu Y_{fuel} - Y_{oxidizer} + Y_{oxidizer}^0}{\nu Y_{fuel}^0 + Y_{oxidizer}^0} \quad (3.50)$$

where  $\nu = \frac{\nu_{oxidizer} \cdot W_{oxidizer}}{\nu_{fuel} \cdot W_{fuel}}$ .

As seen, the mixture fraction is equal to 1 on the fuel zone, and equal to 0 on the oxidizer zone.  $Y_{fuel}^0$  and  $Y_{oxidizer}^0$  are the mass fractions of fuel and oxidizer in a pure fuel and oxidizer streams, respectively. When  $\nu Y_{fuel} = Y_{oxidizer}$ , mixture is in stoichiometric conditions  $Z_{st}$ .

This type of flames are commonly used on the industry. They are safer than premixed flames because avoid the propagation through the inlet. Even so, efficiency is reduced due to its dependence on diffusion, which limits the kinetics of the chemical reactions and also the total heat released.



### 3.7. Verification – Premixed Flames

With the aim of verifying the implementation of the species transport equation and chemical mechanisms, different tests are carried out. Results are verified with a reference solution from Fiorina et. al. [14] and used to compare the effect of the chemical mechanisms on stability, flame speed, temperature, shapes and species evolution.

The premixed flame test consists on studying the behavior of methane/air flame in a two dimensional burner. A mixture of fuel and air is injected through a 4 mm inlet with a parabolic distribution while combustion products are extracted trough a 12 mm outlet. Physical walls of the burner correspond to isothermal walls. All of them are at a constant temperature of 298.15 K. No gravity forces are considered.

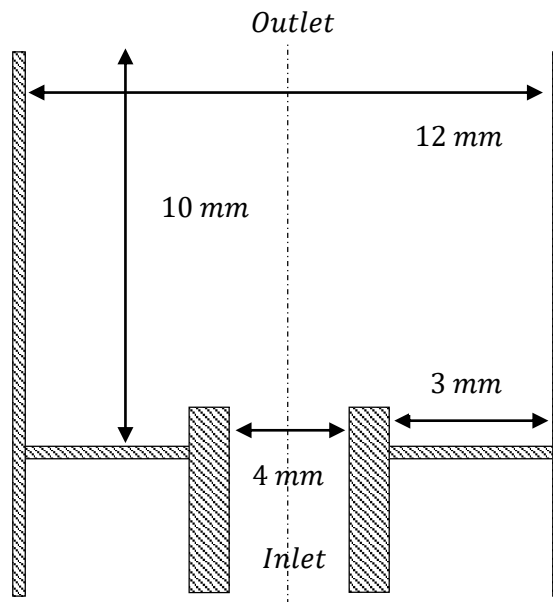


**Figure 11.** Geometry of the burner used on premixed laminar flames.

As explained before, the thickness of laminar flames is small. This requires fine meshes to capture the flame front and simulate with accuracy the kinetics of the chemical model.

A first estimation of the flame thickness is obtained from the thickness equations ( 3.48 ) and ( 3.49 ). The reference flame speed is 1.1 m/s (the same used by Fiorina et. al. [14]) and the maximum temperature is the adiabatic flame temperature at constant pressure and stoichiometric conditions, which is 2223K at 1 bar. Flow properties are evaluated at the inlet.

$$\delta = 2 \cdot 10^{-2} \text{ mm} \quad ( 3.51 )$$

$$\delta_L^0 \approx 0.16 \text{ mm} \quad (3.52)$$

Flame front is only present near the inlet, so grid density is increased in this part of the domain. The minimum grid size of the flame zone is set to  $0.05 \text{ mm}$ . Moreover, due to symmetry only half of the domain is computed, which requires a symmetry boundary condition. This one is defined by one Dirichlet condition to avoid mass flow through the surface and Neumann conditions to the other variables.

As seen on **Figure 12**, grid is refined into different uniform sections. Due to the numerical schemes, an error on the face interpolation is introduced at the edges of each section, but are far away from the flame front and will have a reduced effect on the results.

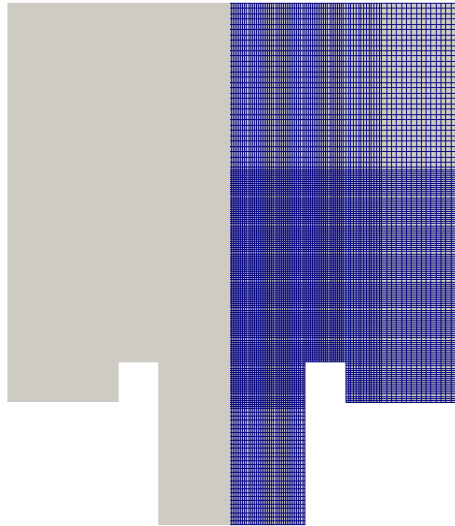


**Figure 12.** Geometry and refined grid of  $90 \times 180 \text{ CV}$ .

To reduce initial instabilities, the flame is initialized with a hyperbolic function centered on a parabola above the inlet. This method is able to initialize the variables in accordance with an existing premixed flame, which avoid ignition issues.

### 3.7.1. Test – Single Step $\text{CH}_4$ / Air Model

Single step mechanism results have shown that inlet velocities lower than  $1.3 \text{ m/s}$  cause flame propagation towards the inlet. This velocity is slightly higher than the one used by Fiorina et. al. [14], which is  $1.1 \text{ m/s}$  with a mechanism of 38 reactions and 14 species.

The laminar flame obtained, described in **Figure 13**, presents the same height and width, and also similar temperature contours as in Fiorina et. al. [14]. Even so, the maximum temperature is slightly higher,  $2130 \text{ K}$  versus  $2098 \text{ K}$  of the reference.

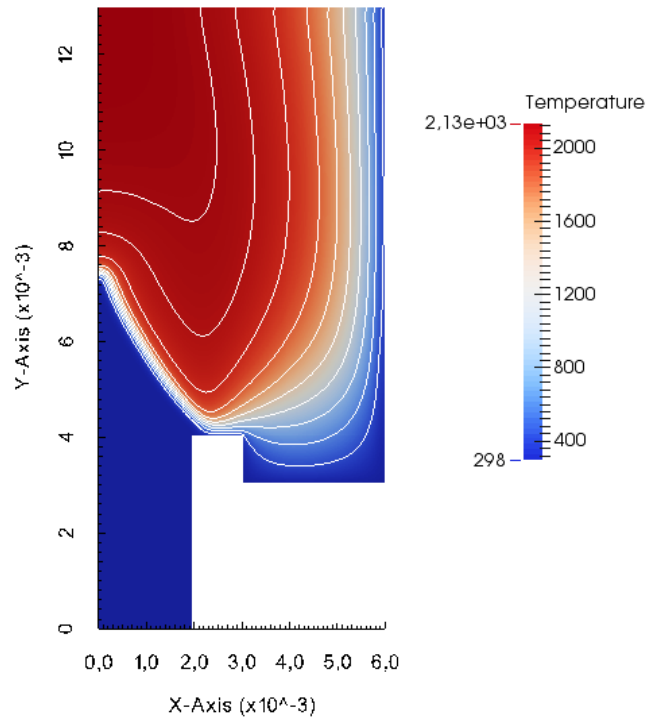


**Figure 13.** Temperature of a single premixed  $\text{CH}_4/\text{Air}$  using a  $90 \times 180$  control volumes (CV) refined mesh.

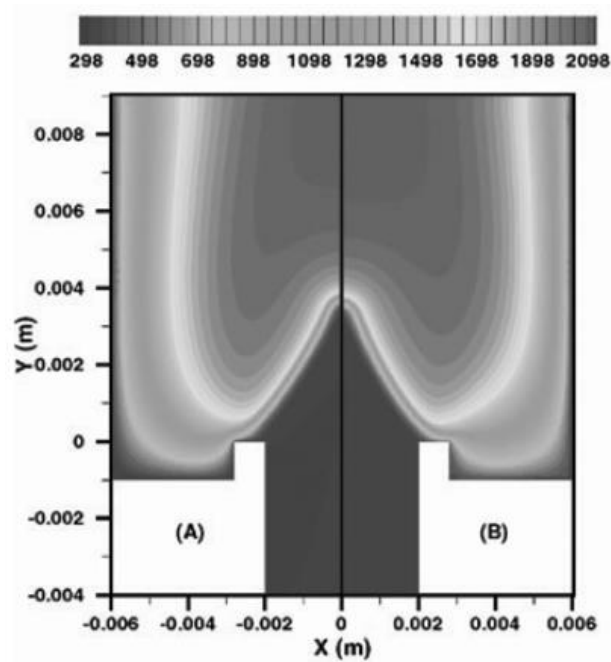


**Figure 14.** Temperature contours of 38 reactions and 14 species mechanism from Fiorina et. al. [14].

Streamlines described in **Figure 15** show that flow crosses perpendicularly to the flame front. The flow experiments an acceleration through the flame, which is related with the density variations due to temperature and concentration changes.

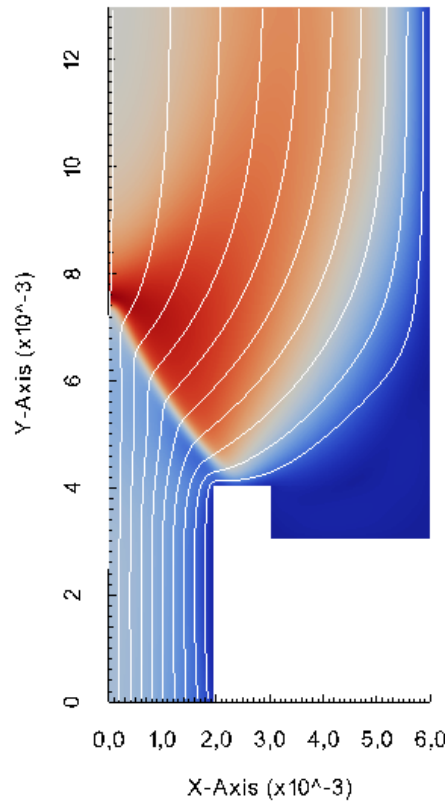


**Figure 15.** Streamlines of single step premixed  $\text{CH}_4/\text{Air}$  using a  $90 \times 180$  CV refined mesh.

The evolution of mass fractions, temperature and rates of production on the axial line at  $x = 0$  shown in **Figure 16** are useful to localize the flame region and its thickness. As it can be seen, chemical reaction occurs on a small region of the domain.

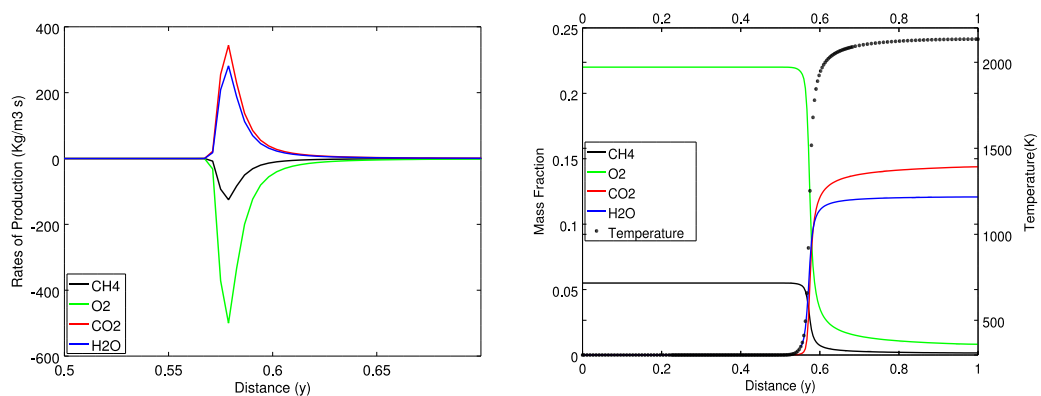


**Figure 16.** Rates of production (left) and mass fractions related with temperature (right) through Y for a single step premixed  $\text{CH}_4/\text{Air}$  using a  $90 \times 180$  CV refined mesh.

This fact is related with the single step mechanism used on the simulation, were final combustion products are directly obtained from the reactants, without any intermediate reaction.

With the aim of verifying the chemical mechanism, radial profiles are plotted at different axial ('Y') positions and compared with results from Fiorina et. al. [14] in **Figure 17**, **Figure 18** and **Figure 19**. Three different radial profiles are exposed.

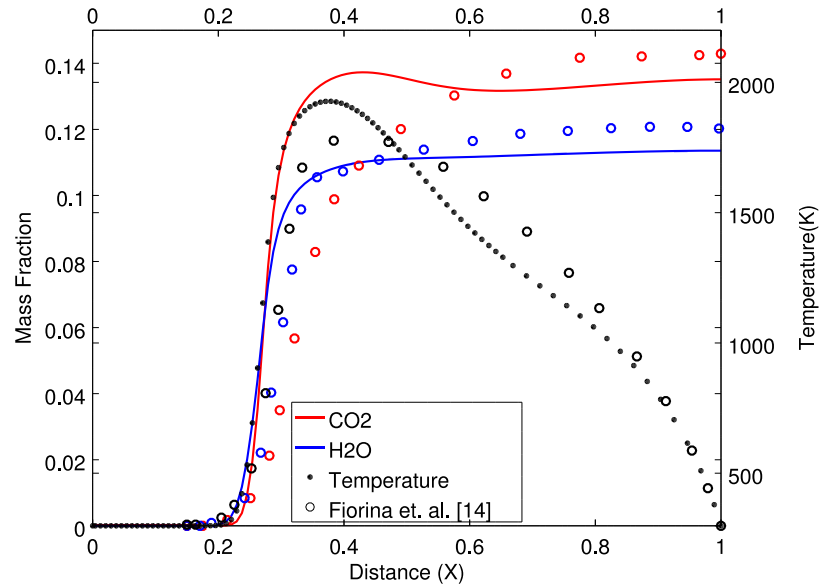


**Figure 17.** Radial profiles of temperature and mass fractions of  $H_2O$  and  $CO_2$  at  $y = 0.003$  for a single step premixed  $CH_4/Air$  using a  $90 \times 180$  CV refined mesh.

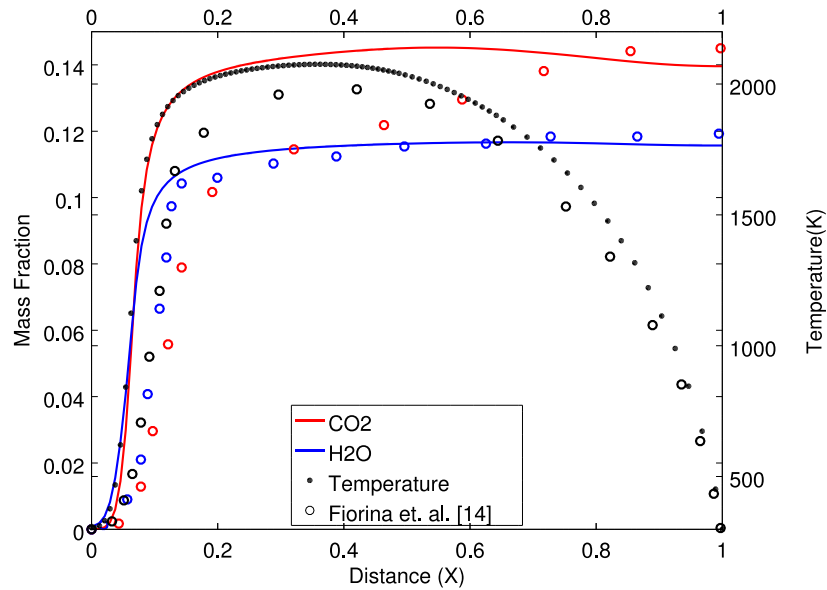


**Figure 18.** Radial profiles of temperature and mass fractions of  $H_2O$  and  $CO_2$  at  $y = 0.007$  for a single step premixed  $CH_4/Air$  using a  $90 \times 180$  CV refined mesh.

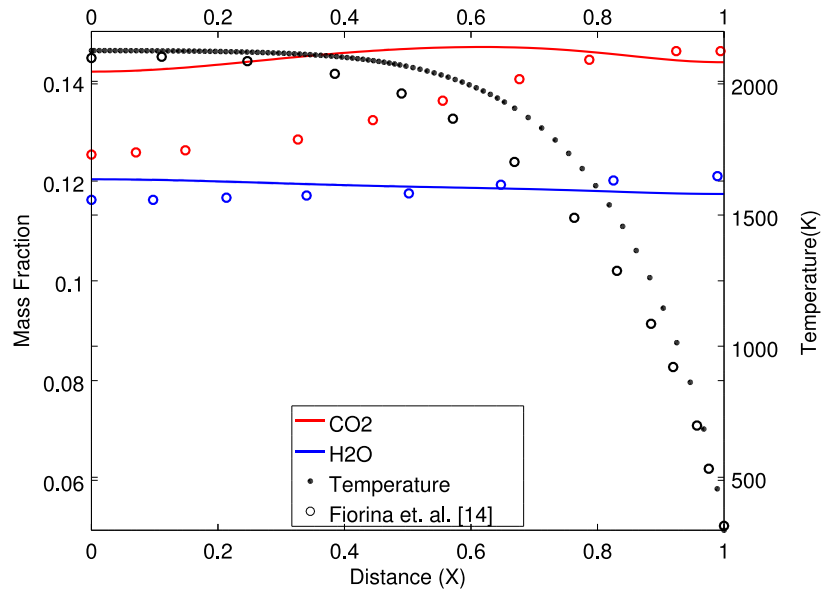


**Figure 19.** Radial profiles of temperature and mass fractions of  $H_2O$  and  $CO_2$  at  $y = 0.011$  for a single step premixed  $CH_4$ /Air using a  $90 \times 180$  CV refined mesh.

It can be seen that temperatures obtained with the single step chemical mechanism are slightly higher than the expected ones, with an important difference on the carbon dioxide mass fraction. Both effects are related with the chemical mechanism. Due to the one and unique chemical reaction, reaction occurs too fast. Products appear before the expected zone and rapidly reach the final mass fraction. Lack of accuracy on mass fractions is related with the existence of other intermediate species that take an important role on the flame front, such as  $CO$ . The addition of more species may include new chemical reactions with less heat release that could modify the temperature profiles and improve the results.

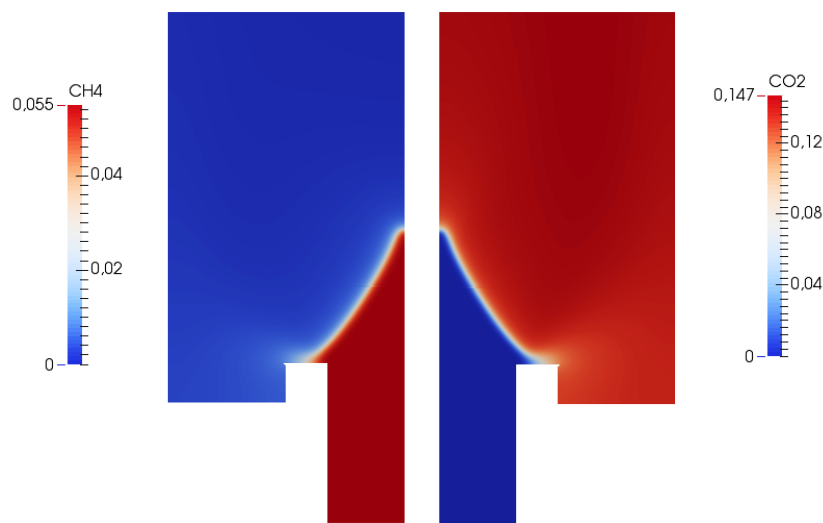


**Figure 20.** Mass fractions for a single step premixed  $CH_4$ /Air using a  $90 \times 180$  CV refined mesh ( $CH_4$ -left and  $CO_2$ -right).

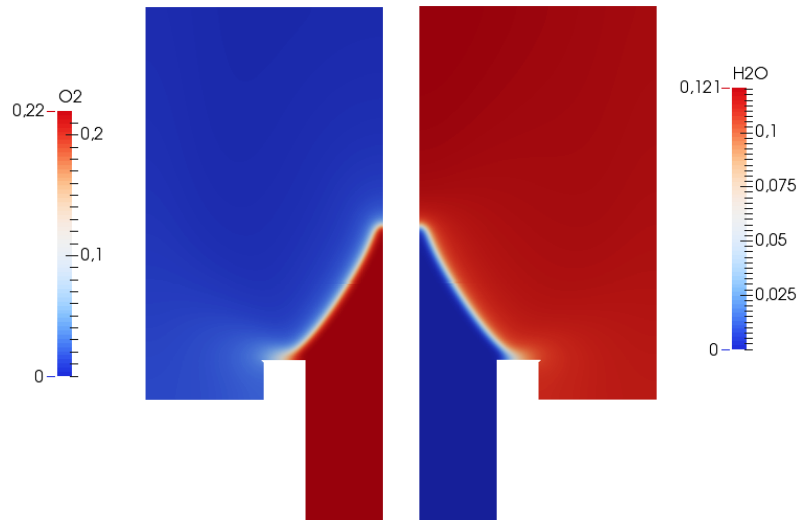


**Figure 21.** Mass fractions for a single step premixed  $CH_4$ /Air using a  $90 \times 180$  CV refined mesh ( $O_2$ -left and  $H_2O$ -right).

The mass fraction of all species included on the single step chemical mechanism are shown in **Figure 20** and **Figure 21**. The small thickness of the flame front can be observed and also the effects of the burner contours on the flame. Due to its temperature of  $298.15\text{ K}$  the flame front cannot touch the surface, and a small quantity of  $CH_4$  and air pass into the domain without burning.

The single step chemical mechanism presents some deficiencies on the temperature estimation, and also on the flame characterization. It has been shown that they are related with the lower quantity of species and also reactions in comparison with more complex chemical mechanisms. Nevertheless, reasonably accurate results are obtained, which can be used as initialization for more complicated mechanisms.

### 3.7.2. Test – Four Steps $CH_4$ / Air Model

The four step mechanism results have shown that inlet velocities higher than  $1.0\text{ m/s}$  result flame propagation towards the outlet. This velocity is slightly lower than the one used by Fiorina et. al. [14], which is  $1.1\text{ m/s}$ . Temperature profiles, velocity streamlines and also mass fractions for each species are presented in the following figures.

The laminar flame obtained, shown in **Figure 22**, presents the same height and width, and also similar temperature contours as the ones shown by Fiorina et. al. [14]. Even so, the maximum temperature is slightly higher,  $2140\text{ K}$  versus  $2098\text{ K}$  of the reference.

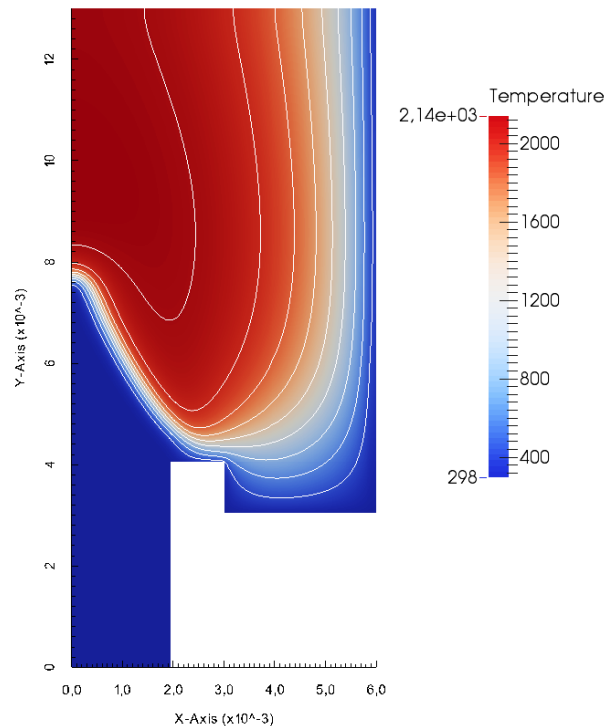


**Figure 22.** Temperature of four step premixed  $CH_4$ /Air using a  $90 \times 180$  CV refined mesh.

Streamlines described in **Figure 23** for four steps and single step cases are quite similar, and in both cases velocity crosses perpendicular to the flame front.

Evolution of species and rates of production on the axial line at  $x = 0$  described in **Figure 24** shows the four steps mechanism. Combustion of the fresh gas starts with the formation of  $CO$  and  $H_2$ . As a second step,  $CO$  and  $H_2$  react and become  $CO_2$  and  $H_2O$ , respectively. This can be seen on the rates of progress, where there is a positive zone (production) followed by a negative zone (destruction). The negative rates of reactions coincide with the positive rates of  $CO_2$  and  $H_2O$ , respectively.



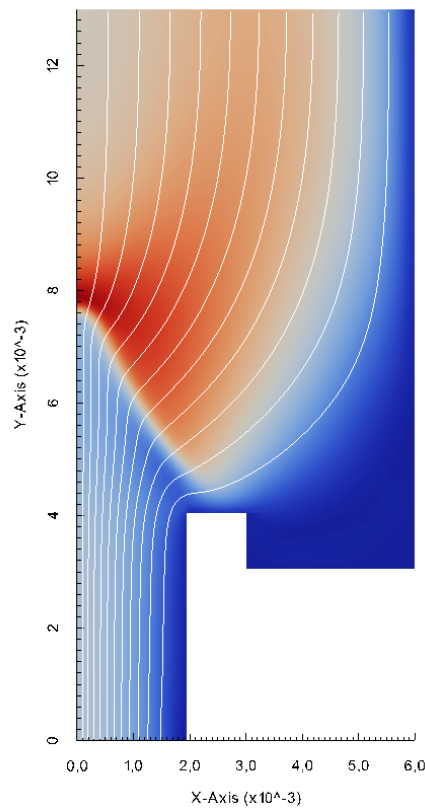


**Figure 23.** Streamlines of four step premixed  $CH_4$ /Air using a  $90 \times 180$  CV refined mesh.

Is interesting to note the elevated rate of reaction of  $CO$  and the peak on its mass fraction on the flame front.

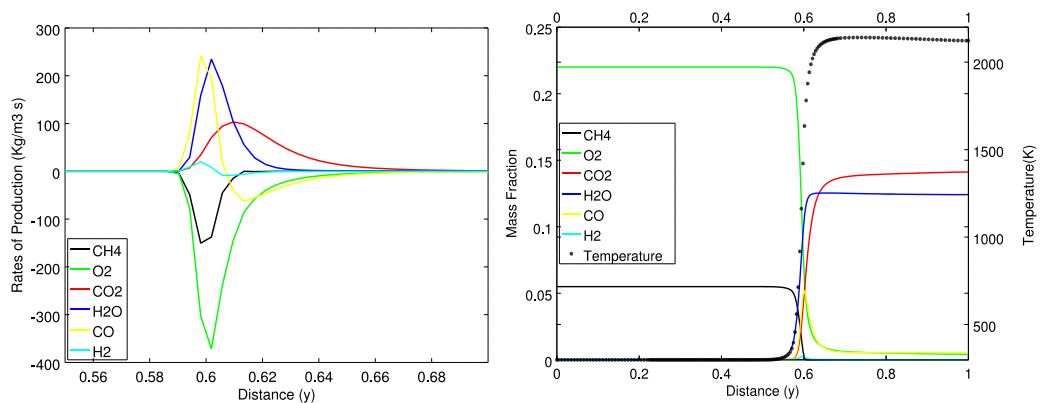


**Figure 24.** Rates of production (left) and mass fractions related with temperature (right) through  $Y$  of a four step premixed  $CH_4$ /Air using a  $90 \times 180$  CV refined mesh.

With the aim of analyzing the chemical mechanism, results are plotted through radial profiles and compared against results from Fiorina et. al. [14] and results from the single step in **Figure 25**, **Figure 26** and **Figure 27**.

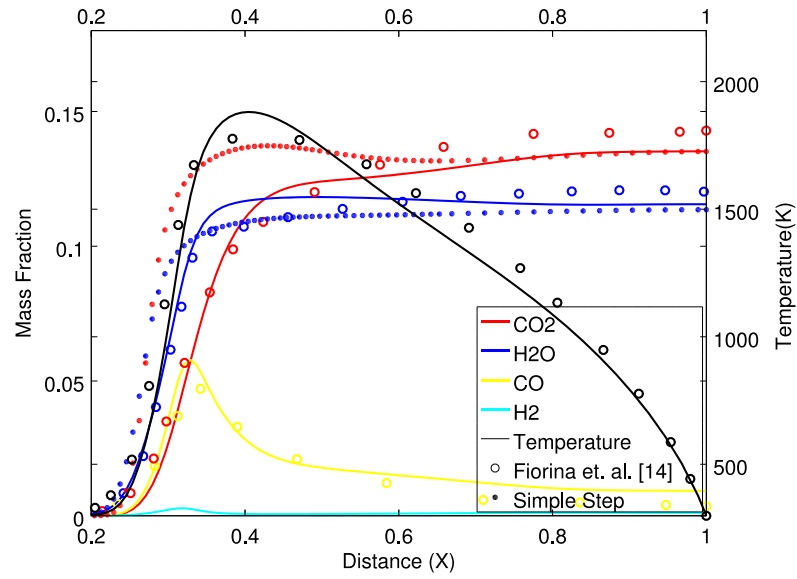


**Figure 25.** Radial profiles of temperature and mass fractions of  $H_2O$  and  $CO_2$  at  $y = 0.003$  of four step (lines) and single step (dots) premixed  $CH_4$ /Air using a  $90 \times 180$  CV refined mesh.

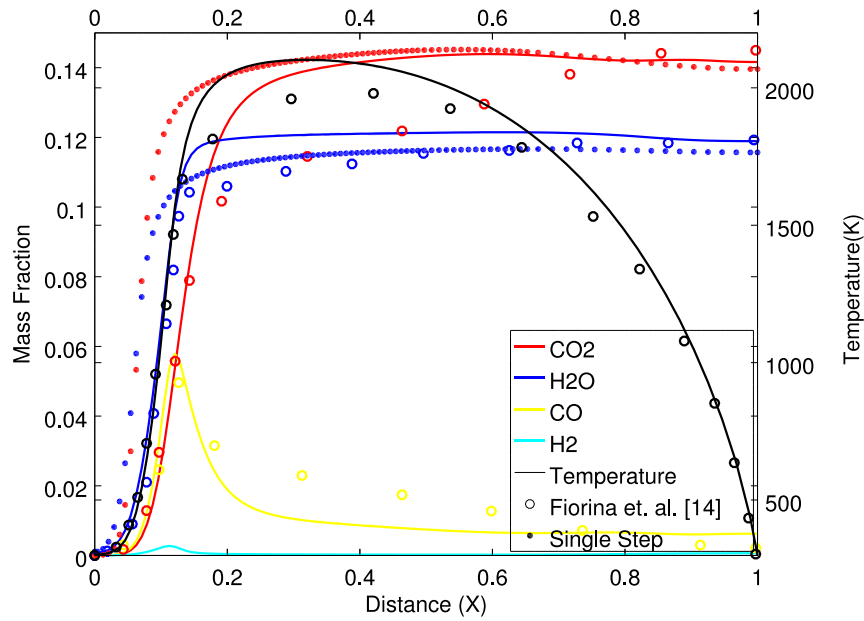


**Figure 26.** Radial profiles of temperature and mass fractions of  $H_2O$  and  $CO_2$  at  $y = 0.007$  of four step (lines) and single step (dots) premixed  $CH_4$ /Air using a  $90 \times 180$  CV refined mesh.

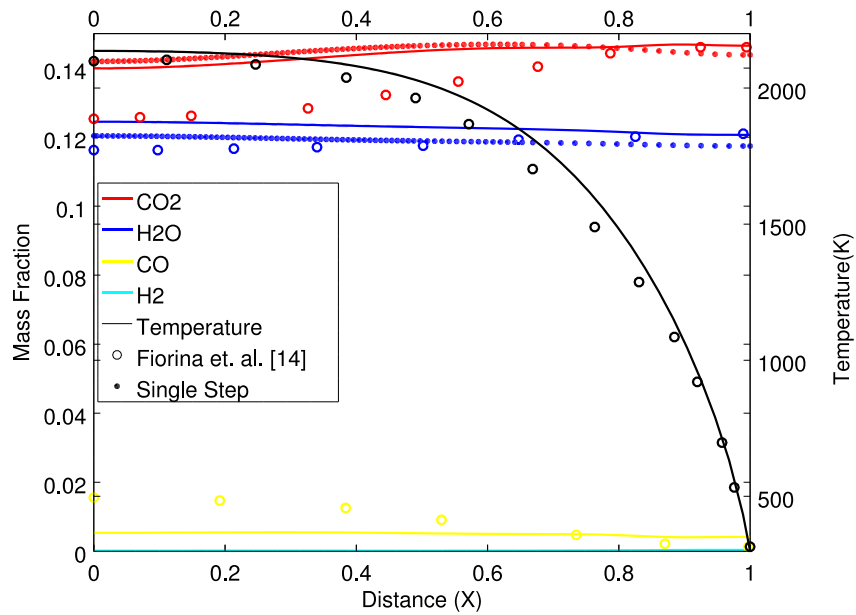


**Figure 27.** Radial profiles of temperature and mass fractions of  $H_2O$  and  $CO_2$  at  $y = 0.011$  of four step (lines) and single step (dots) premixed  $CH_4/Air$  using a  $90 \times 180$  CV refined mesh.

The introduction of  $CO$  and  $H_2$  leads to an important increase on accuracy. Prediction of the mass fractions at the beginning of the combustion process is extremely accurate for the presence of these new species. Mass fractions increase near the flame front, followed by a smooth reduction of the intermediate species due to reversible reactions. This effect is clearly seen in **Figure 25** and **Figure 26**.

In addition, it can be seen that  $CO$  and  $CO_2$  present an important error after the  $CO$  peak. This error is increased away from the burner wall, where the temperature reaches its highest value. This could mean that the four steps chemical mechanism produces too much  $CO_2$  at high temperatures, and maybe other reactions that involve  $CO$  and  $CO_2$  must be introduced on the scheme. Even so, temperature profiles are improved.

Besides chemical mechanism, the difference on the mass fractions values could be related with the molecular diffusions simplifications. This term is neglected on the energy equation, and also a simplification is introduced on the species transport equation.

In **Figure 28**, **Figure 29** and **Figure 30**, mass fractions of all species included on the four step chemical mechanism are shown.

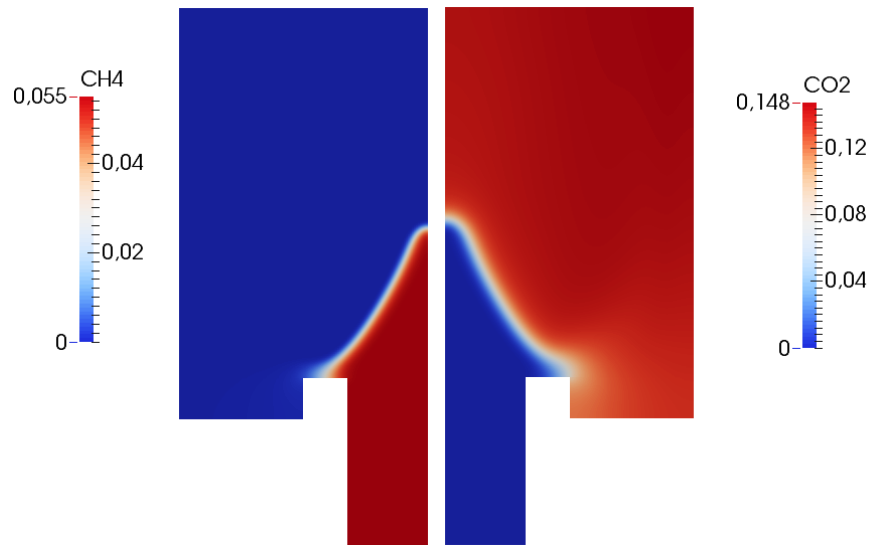


**Figure 28.** Mass fractions for a four step premixed  $CH_4$ /Air using a  $90 \times 180$  CV refined mesh ( $CH_4$ -left and  $CO_2$ -right).

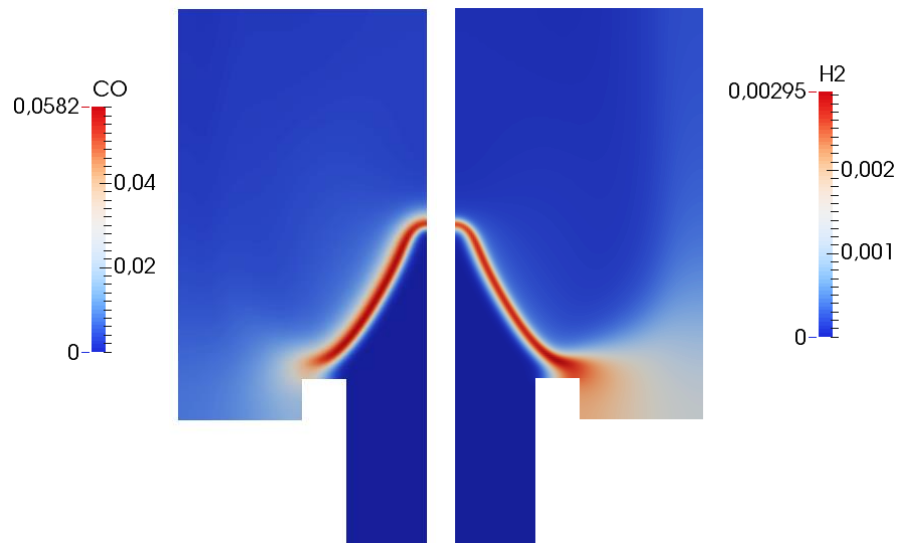


**Figure 29.** Mass fractions for a four step premixed  $CH_4$ /Air using a  $90 \times 180$  CV refined mesh ( $CO$ -left and  $H_2$ -right).

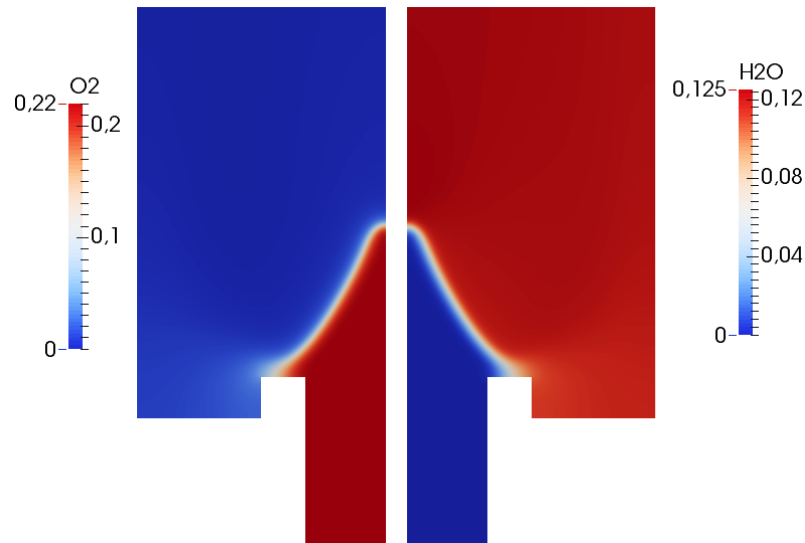


**Figure 30.** Mass fractions for a four step premixed  $CH_4$ /Air using a  $90 \times 180$  CV refined mesh ( $O_2$ -left and  $H_2O$ -right).

The four step chemical mechanism presents better accuracy than the single step. The addition of two reactions and two species to the single step mechanism increases slightly the computational time, but also the accuracy on the results. Some deficiencies on mass fractions can still be observed at the middle and end of the flame front, with an error on the temperature profile in the same region. Nevertheless, it gives reasonably accurate results on the temperature estimation with low computational requirements.

## 4. Turbulence Modelling

### 4.1. Introduction

Industrial applications require the study of reacting flows with short combustion times and fast mixing processes. These requirements usually imply complicated flow patterns and also turbulent flows. Turbulent flows are characterized by a large span of spatial scales. The largest spatial scales of turbulence transport the energy to the smallest ones, while the smallest ones are dissipated into heat. The resolution of all these scales is necessary to ensure that the final results are close to the reality. Usually meshes required to capture all the scales are very small, which increases the computational time.

With the aim of reducing it, different models have been introduced, such as Reynolds Average Navier – Stokes equations (RANS) and Large Eddy Simulations (LES). On the one hand, RANS are time – averaged equations that computes a time averaged values for each variable of study. On the other hand LES models are based on a spatial filtering to filter out the small scales of the flow and only solve the largest spatial scales. The small scales are modeled through the gradient – diffusion hypothesis by introducing a turbulent viscosity. This reduces the flow scales to be computed which leads to being able to use coarser meshes and lower computational requirements.

Applications of LES models to reacting flows were introduced in the early 1990s, and it has been applied to different cases of interest, as aircraft engine combustions [15]. There is an obvious interest to apply LES instead of RANS models due to its capacity to capture the local flow behavior and unsteady phenomena.

This chapter focuses on the application of LES to turbulent combustion phenomenon, models to predict the subgrid scale and also the particularities of combustion modelling on turbulent flows.

## 4.2. Large – Eddy Simulation

### 4.2.1. Temporal Average

As exposed before, LES provides more information than RANS due to its capacity to capture the flow behavior. Therefore, it is difficult to compare turbulent results due to its fluctuations. Time average methods are highly used to express stationary turbulence in terms of a mean and a fluctuation part. The application of these methods on variable density flows requires special attention due to correlation issues [16].

#### 4.2.1.1. Reynolds Average

The averaging concept was introduced by Reynolds in 1895. A time average of a turbulent flow based on the Reynolds averaging consists on decompose a variable into a time-averaged part and a fluctuation part. If flow variable is defined as  $f(x, t)$ , the time average is computed with the equation ( 4.1 ).

$$F(x) = \lim_{T \rightarrow \infty} \frac{1}{T} \int_t^{t+T} f(x, t) dt \quad (4.1)$$

For stationary turbulence, flow variables are defined as the sum of a mean and a fluctuation part.

$$f(x, t) = F(x) + f'(x, t) \quad (4.2)$$

In this case, the time average of the fluctuation variable is equal to zero because  $F(x) = \overline{F(x)}$ .

$$f'(x, t) = \lim_{T \rightarrow \infty} \frac{1}{T} \int_t^{t+T} [f(x, t) - F(x)] dt = F(x) - \overline{F(x)} = 0 \quad (4.3)$$

Time average equations usually are applied in a specific range of times instead of an infinite one. To avoid fluctuation effects on the mean variable suitable integration times must be used.

The application of the Reynolds average to the governing equations leads to time averages of nonlinear terms. Thus, correlation terms appear on the equations.

$$\overline{\phi\psi} = \overline{\phi\psi} + \overline{\phi\psi'} + \overline{\phi'\psi} + \overline{\phi'\psi'} = \phi\psi + \overline{\phi'\psi'} \quad (4.4)$$

The number of correlations increases as more variables are added on the mean value. In variable density flows, the convective term presents three variables (density and two velocities), which leads to triple correlations. To avoid this, the Favre average is applied.

### 4.2.1.2. Favre Average

For variable density flows, density is also expressed by a mean and fluctuation parts.

$$\rho = \bar{\rho} + \rho' \quad (4.5)$$

As explained before, it introduces a triple correlation on the momentum equation. This problem can be simplified using the density – weighed averaging procedure (Favre average).

$$\overline{f(x)} = \frac{1}{\bar{\rho}} \lim_{T \rightarrow \infty} \int_t^{t+T} \rho(x, t) f(x, t) dt \quad (4.6)$$

where  $\bar{\rho}$  is the Reynolds averaged density. Favre average can be rewritten in terms of the Reynolds average

$$\bar{\rho} \tilde{f} = \overline{\rho f} \quad (4.7)$$

The decomposition on a mean and fluctuation part on the Favre average is done in terms of density and velocity.

$$\overline{\rho f} = \bar{\rho} \tilde{f} + \overline{\rho f''} \quad (4.8)$$

From the Favre average ( 4.7 ) definition  $\overline{\rho f''} = 0$ . This reduces the number of correlations that appear on the governing equations when dealing with variable density.

To compute the mean values the following equation is used, which employs the time step of each iteration and the accumulated mean value.

$$\langle \overline{\rho \phi} \rangle_{n+1} = \frac{(\overline{\rho \phi})_{n+1} \cdot \Delta t + \langle \overline{\rho \phi} \rangle_n \cdot t_a}{t_a + \Delta t} \quad (4.9)$$

Favre average variable can be recovered with the Reynolds averaged density.

$$\langle \tilde{\phi} \rangle = \frac{\langle \overline{\rho \phi} \rangle}{\langle \bar{\rho} \rangle} \quad (4.10)$$



### 4.2.2. LES Equations

Large – Eddy Simulations are used to model the smallest scales of the flow by applying a low pass filter to the low – Mach equations.

$$\overline{\rho\phi} = \int_{\Omega} \rho\phi G(x, \xi) d\xi \quad (4.11)$$

where  $G(x, \xi)$  is the Kernel filter. As it can be seen, the overbar in this section denotes spatial filtering. The low-Mach equations after the application of the filter are the following ones.

$$\frac{\partial \bar{\rho}}{\partial t} = -\frac{\partial(\bar{\rho}\tilde{u}_j)}{\partial x_j} \quad (4.12)$$

$$\frac{\partial(\bar{\rho}\tilde{u}_i)}{\partial t} = -\frac{\partial(\bar{\rho}\tilde{u}_j\tilde{u}_i)}{\partial x_j} - \frac{\partial \bar{p}}{\partial x_i} + \frac{\partial}{\partial x_j} \left( (\bar{\mu} + \bar{\mu}_t) \bar{\sigma}_{ij} \right) + \bar{\rho} g_i \quad (4.13)$$

$$\bar{\rho} c_p \frac{\partial \tilde{T}}{\partial t} = -\bar{\rho} c_p \tilde{u}_i \frac{\partial \tilde{T}}{\partial x_i} + \frac{\partial}{\partial x_i} \left( (\bar{\lambda} + \bar{\lambda}_t) \cdot \frac{\partial \tilde{T}}{\partial x_i} \right) + \bar{\omega}_T \quad (4.14)$$

$$\bar{\rho} \frac{\partial \tilde{Y}_k}{\partial t} = -\bar{\rho} \tilde{u}_i \frac{\partial \tilde{Y}_k}{\partial x_i} + \frac{\partial}{\partial x_i} \left( \bar{\rho} (\bar{D}_k + \bar{D}_{k_t}) \cdot \frac{\partial \tilde{Y}_k}{\partial x_i} \right) + \bar{\omega}_k \quad (4.15)$$

where  $\bar{\sigma}_{ij} = \left( \frac{\partial \tilde{u}_i}{\partial x_j} + \frac{\partial \tilde{u}_j}{\partial x_i} - \frac{2}{3} \delta_{ij} \frac{\partial \tilde{u}_k}{\partial x_k} \right)$ . The unresolved scales are modeled through the gradient – diffusion hypothesis by introducing a turbulent viscosity.

$$2\bar{\mu}_t \left( \bar{S}_{ij} - \frac{1}{3} \delta_{ij} \nabla \tilde{u} \right) \approx \nabla(\bar{\rho} \tilde{u} \tilde{u}) - \nabla(\bar{\rho} \overline{uu}) \quad (4.16)$$

Where  $\bar{S}_{ij}$  is the strain stress tensor defined as  $\bar{S}_{ij} = \frac{1}{2} \left( \frac{\partial \tilde{u}_i}{\partial x_j} + \frac{\partial \tilde{u}_j}{\partial x_i} \right)$ . There are many models to compute the turbulent viscosity, but in this study the Smagorinsky model is used.

Turbulent conductivity ( $\bar{\lambda}_t$ ) and molecular diffusivity ( $\bar{D}_{k_t}$ ) are expressed in terms of the turbulent viscosity by using the turbulent Prandtl ( $Pr_t$ ) and the turbulent Schmidt number ( $Sc_t$ ).

$$Pr_t = \frac{\bar{\mu}_t c_p}{\bar{\lambda}_t} \quad (4.17)$$

$$Sc_t = \frac{\bar{\mu}_t}{\rho D_{k_t}} \quad (4.18)$$

Both numbers for turbulent flows are set equal to 0.7 [17].

#### 4.2.3. Smagorinsky Model

The Smagorinsky model proposed by Joseph Smagorinsky in 1963 [18] consists on computing the turbulent viscosity from the strain tensor.

$$\bar{\mu}_t = \rho (C_s \Delta)^2 |\tilde{S}| \quad (4.19)$$

where  $|\tilde{S}| = \sqrt{2 \cdot \tilde{S}_{ij} \cdot \tilde{S}_{ij}}$ ,  $\Delta$  is the grid size and  $C_s$  the Smagorinsky constant, usually 0.18.

As it can be seen, it depends on the velocity gradient at the cell center. Segarra et. al. [19] show the importance of getting accurate gradient evolutions and also presents two common methods to compute it. The first one is based on the Green – Gauss theorem and the other one is the least – squares method. It is known that the second one offers better accurate results, but for the purposes and schedule of this study, the Green – Gauss is selected.

$$\nabla \phi_p \approx \frac{1}{V_p} \int_{V_p} \nabla \phi dV = \frac{1}{V_p} \int_A \phi d\vec{A} \approx \frac{1}{V_p} \sum \phi_f \vec{A}_f \quad (4.20)$$

where  $x$  index represents the cell faces. Variable  $\phi_f$  at the face cell is not known, so numerical schemes of section 2.3.2 can be used to estimate it. In this case, the CDS scheme for structured meshes is selected due to simplicity on its application.

### 4.3. Eddy Dissipation Combustion

In turbulent flows, the smallest eddies transform the kinetic energy into heat due to the work done by molecular forces, while the largest eddies transport the kinetic energy to the smallest scales. The introduction of the heat release at the small scales and its effect on the chemical kinetics is done through the eddy dissipation mode (EDM) defined by Magnussen [20] on the 1970s. In this study, an adaptation of the initial EDM extended to simulate combustions considering fast chemistry within LES proposed by Howard et. al. [17] is used.

$$\omega_{EDM} = AC_\mu \rho \frac{\bar{\kappa}}{\bar{\mu}_{EDM}} \min(v_f Y_f, v_o Y_o) \quad (4.21)$$

where index  $f$  refers to fuel,  $o$  to oxidizer,  $p$  to products,  $\bar{\kappa}$  to the subgrid turbulence kinetic energy, which divided by the turbulent viscosity gives a subgrid local turbulent inverse time scale and  $C_\mu$  to the subgrid model. For this application, the turbulent viscosity has a particular model that differs from the Smagorinsky.

$$\bar{\mu}_{t_{EDM}} = \frac{2}{3} \rho C_k^{-\frac{3}{2}} \cdot \left[ \frac{\bar{\kappa}}{\pi} \cdot \Delta \right] \quad (4.22)$$

where  $C_k = 2.1$  (Kolmogorov constant). The turbulent kinetic energy for the Smagorinsky model is computed as follows.

$$\bar{\kappa} = \left( \frac{C_s^2}{0.094} \right)^2 \cdot \Delta^2 \cdot |\bar{S}|^2 \quad (4.23)$$

The total reaction rate is obtained from the sum of the turbulent mixing scale and chemical reaction time scale. Both of them are obtained from the inverse of the EDM and Arrhenius reaction rates (in seconds).

$$\frac{1}{\omega_T} = \frac{1}{\omega_{EDM}} + \frac{1}{\omega_A} \quad (4.24)$$

where  $\omega = \frac{\dot{\omega}}{\rho}$ . This expression is modified to get the following one.

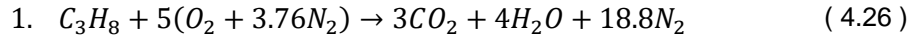
$$\omega_T = \frac{\omega_A \cdot \omega_{EDM}}{\omega_A + \omega_{EDM}} \quad (4.25)$$

At this point, the Arrhenius law and the eddy dissipation model could be related with the reactions of the resolved part and the subgrid part, respectively. The first

one uses the resolved variables while the second one uses an approximation based on the turbulent kinetic energy of the subgrid scales.

#### 4.3.1. Single Step $C_3H_8$ / Air Model

The chemical mechanism used on further simulations consists on a single step  $C_3H_8$  / Air combustion.



The chemical mechanism is the same one as used by Howard et. al. [17]. As explained before, two different rates of production are evaluated, each one with specific coefficients. For the Arrhenius rate of production, the following coefficients are applied.

**Table 13.** Coefficients applied on the Arrhenius equation.

<i>Reaction</i>	$A \left( \frac{m^3}{kg \cdot s} \right)$	$\beta$	$Ea/R \text{ (K)}$
1	$10^{10}$	0.0	18400

For the eddy dissipation model, the following coefficients are applied.

**Table 14.** Coefficients applied on the EDM equation.

<i>Reaction</i>	$A$	$C_k$
1	4	2.1

Molar mass of the species added on this chemical mechanism are the following.

**Table 15.** Molar mass of added species on the four step mechanism.

<i>Species</i>	<i>Molar Mass (kg/mol)</i>
$C_3H_8$	$0.4409721088e - 1$

The selection of  $C_\mu$  coefficient of the EDM model has a direct impact on the flame stability. Higher values displace the flame front to the inlet, while lower values tend to extinguish the flame inside the burner and in some cases, avoid the ignition. Howard et. al. [17] exposes that this value could be related with the LES model applied.

Due to the fact that coefficients are in mass, the stoichiometric coefficients on the EDM equation ( 4.21 ) are set to 1 and 17 respectively, in accordance with the reference ones [17].

#### 4.4. Application

In this section the study of a turbulent combustion of propane inside a three dimensional burner is exposed. With the aim of comparing the results a simple burner geometry is selected, which numerical and experimental results are available from Howard et. al. [17] and Legier [21].

##### 4.4.1. $C_3H_8$ / Air Non-premixed Burner

The non-premixed burner simulation consist on studying the behavior of a diffusion flame of propane and air as fuel and oxidizer into a three dimensional burner. Both species are injected through different inlets into the burner, which its geometry creates a flame known as lifted flame. Due to symmetry, only half of the burner is computed. Fuel is injected through a  $4 \times 30 \text{ mm}$  inlet, while air is injected through two inlets, the first one of  $12 \times 30 \text{ mm}$  and the second one of  $7 \times 30 \text{ mm}$ . A thin wall of  $1 \text{ mm}$  of thickness keeps both flows separated  $10 \text{ mm}$  before mixing.

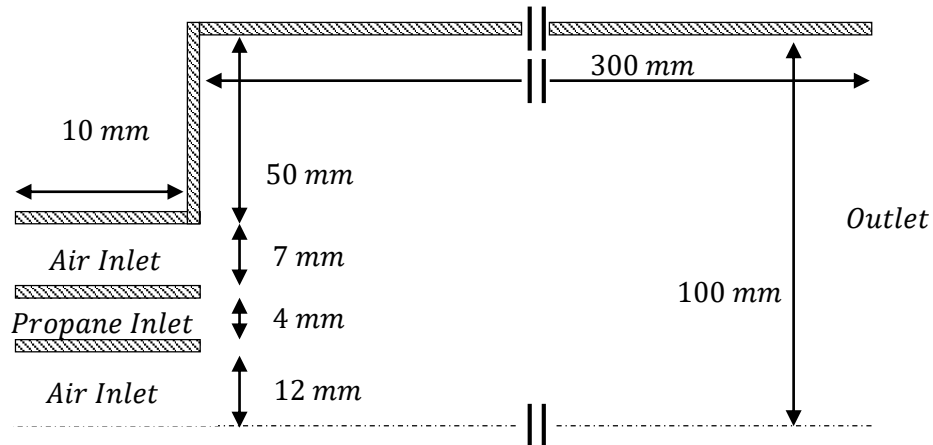


**Figure 31.** Geometry of the burner used on the turbulent non premixed flame.

Due to the fact that turbulent flows are not steady, it is difficult to guess the final position of the flame into the burner. For this reason, a uniform mesh of  $166 \times 100 \times 20$  is used.

The HDS numerical scheme is used on the scalar equations. CDS and QUICK schemes show instabilities that produces undesired effects and unreal results. As explained on section 2.3.2.3, a SP scheme is applied on the momentum equations to preserve the global kinetic energy.

All physical walls are adiabatic with a nonslip condition and no normal velocity through them. Dynamic pressure is set to zero at the outlet and free on the inlet. To emulate continuity on the covers and on the symmetry plane, a symmetry condition is imposed. Thermodynamic pressure is set to atmospheric pressure.

Fuel inlet velocity is set to  $4.5 \text{ m/s}$  while oxidizer inlet velocity is set to  $18 \text{ m/s}$ . Both flows are at  $298.15 \text{ K}$ .

On the following figure a three dimensional representation of the propane burner is exposed.

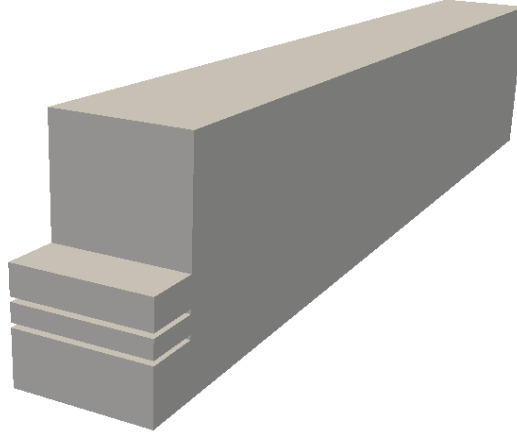


**Figure 32.** Three dimensional view of the domain that defines the propane burner.

At the initial time, all the domain is feed with nitrogen at  $2000 \text{ K}$  to ensure the ignition of reactants. After  $0.01$  seconds, the Favre average starts to compute the mean values and ends at  $0.15$  seconds, time enough for the flow to cross the burner several times. This limitation is also introduced to reduce the computational time required.

In this case, several tests show that a minimum value of  $C_\mu = 0.7$  can be used to keep the combustion inside the burner. Results for  $C_\mu = 0.7$  are exposed, which include the mean rates of production, mean mass fraction of reactants and mean temperature on the middle plane. Moreover, a comparison of vertical profiles with experimental and numerical data from references are described.

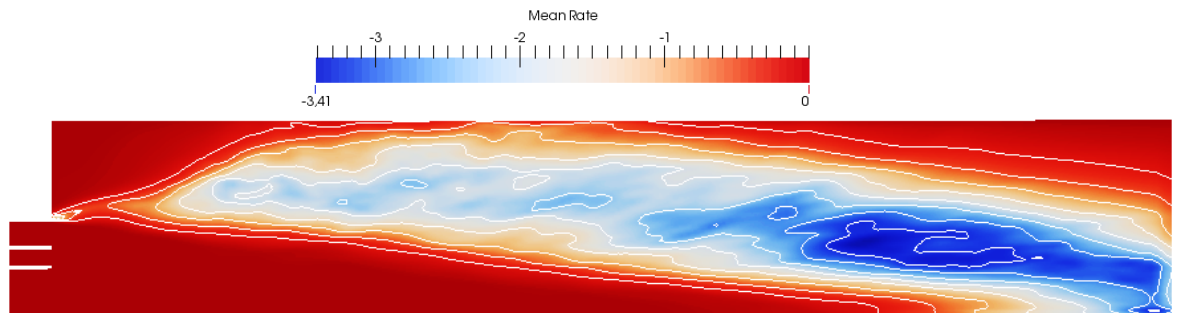


**Figure 33.** Mean reaction rates contours ( $\text{kg/m}^3\text{s}$ ) of propane for turbulent  $\text{C}_3\text{H}_8/\text{Air}$  using a  $166 \times 100 \times 20$  CV mesh.

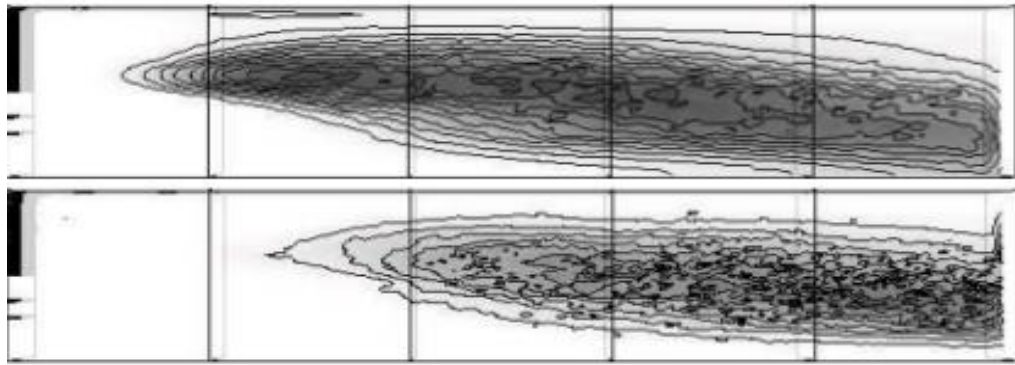


**Figure 34.** Mean reaction rates contours at the middle plane (each  $0.25 \text{ kg/m}^3\text{s}$  from 0 to  $3 \text{ kg/m}^3\text{s}$ ) with Wale model ( $125 \times 100 \times 15$  CV the first one and  $166 \times 100 \times 20$  CV the second one) from Howard et. al. [17].

The highest rates are found at the middle-end of the burner, while the maximum mean rate of propane is  $3.41 \text{ kg/m}^3\text{s}$ , slightly higher than  $3 \text{ kg/m}^3\text{s}$  from Howard et. al. [17].

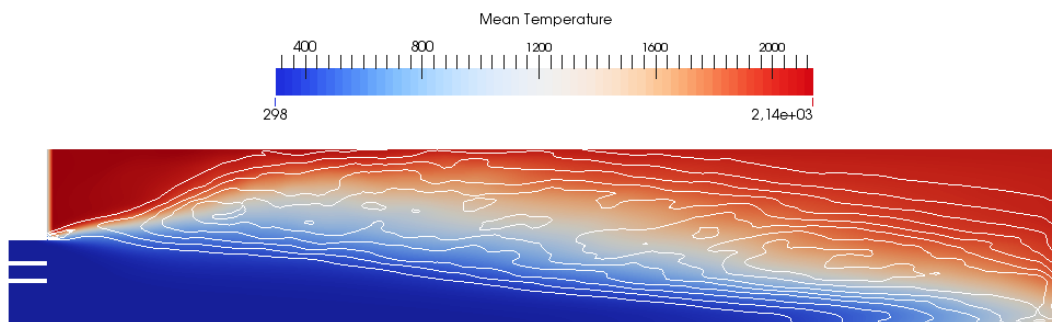


**Figure 35.** Mean temperature (K) for turbulent  $\text{C}_3\text{H}_8/\text{Air}$  using a  $166 \times 100 \times 20$  CV mesh.

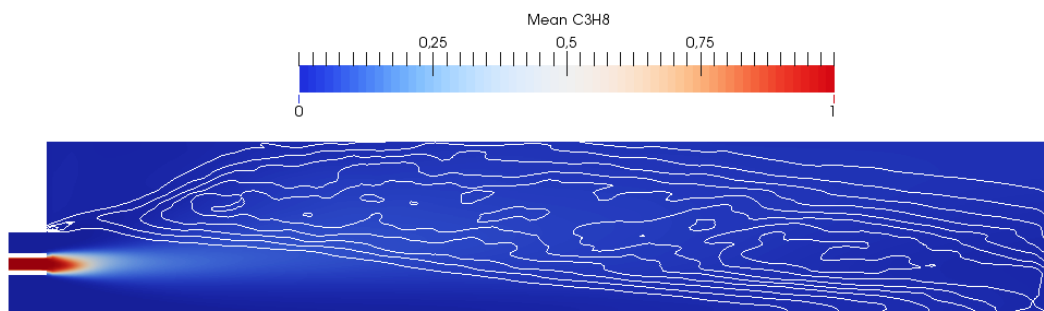


**Figure 36.** Mean mass fraction of propane for turbulent  $\text{C}_3\text{H}_8/\text{Air}$  using a  $166 \times 100 \times 20$  CV mesh.

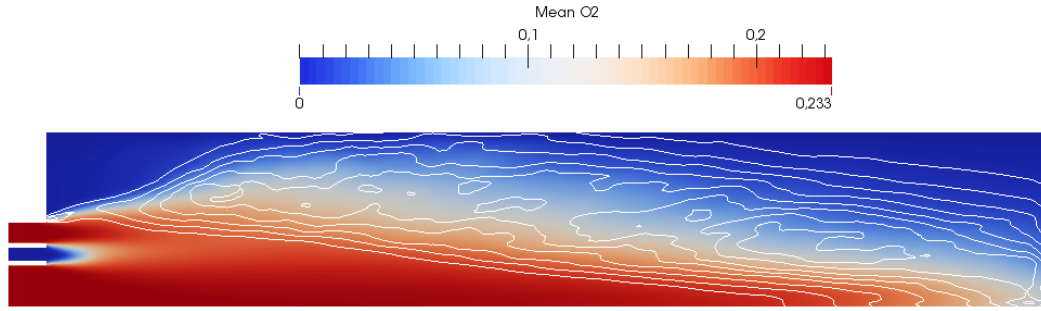


**Figure 37.** Mean mass fraction of oxygen for turbulent  $C_3H_8$ /Air using a  $166 \times 100 \times 20$  CV mesh.

The flame front is localized at the middle – end of the burner, where premixed conditions of fuel and air are achieved. Before this zone, the mixture is too lean and low reaction rates are found. At the beginning of the burner there appears a recirculation of hot gases. This recirculation captures part of the downstream diffused propane, which produces a partial combustion near the upper air inlet.

Profiles at two different locations are presented. The first profile corresponds to a vertical line at  $x = 0.004 \text{ m}$  and the second one to a vertical line at  $x = 0.012 \text{ m}$ , both of them at  $z = 0.015 \text{ m}$  (middle plane). Mean mass fraction of oxygen and horizontal velocity are compared. As it can be seen, oxygen mass fractions are quite similar to the experimental ones. At  $x = 0.004 \text{ m}$ , the existence of a small combustion near the upper inlet avoids oxygen to reach the upper zone which introduces the main difference with results from Howard et. al. [17]. Even so, velocity profile show similar results with the reference ones. It can be seen the effect of the propane inlet at a lower velocity than air, and negative values related with the recirculation zone on the upper part of the inlet.

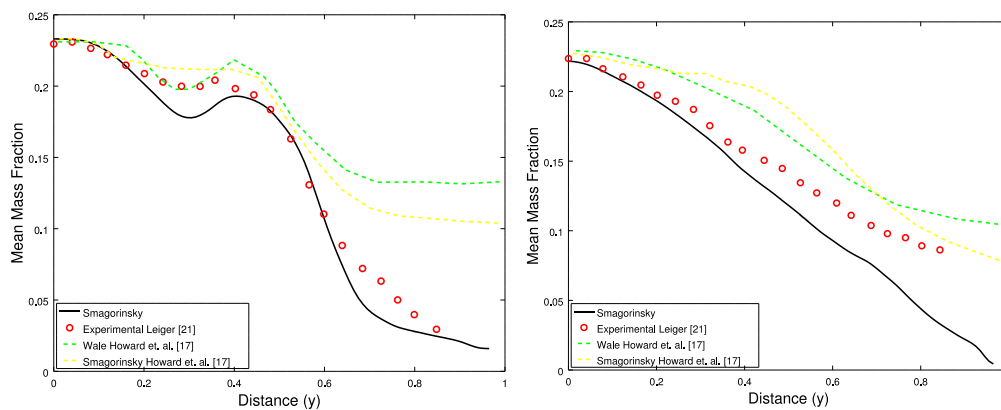


**Figure 38.** Mean mass fraction vertical profiles of oxygen using the Smagorinsky model (line) at  $x = 0.04$  and  $x = 0.12 \text{ m}$  for turbulent  $C_3H_8$ /Air using a  $166 \times 100 \times 20$  CV mesh.

At  $x = 0.012 \text{ m}$ , oxygen mass fraction gives reasonable values. Near the top wall, the difference with the experimental results and also with the numerical results



from Howard et. al. [17] increases. Comparison of velocity profiles is quite difficult. No experimental results are available and Howard et. al. [17] results are very different with a high dependency on the mesh resolution. Moreover, they use a wale model which is more accurate than the Smagorinsky.

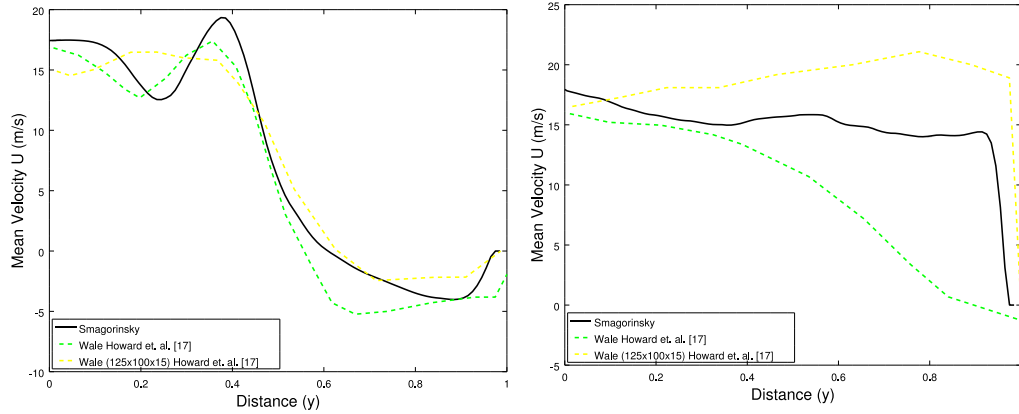


**Figure 39.** Mean profiles of horizontal velocity using the Smagorinsky model (line) at  $x = 0.04 \text{ m}$  and  $x = 0.12 \text{ m}$  for turbulent  $C_3H_8/\text{Air}$  using a  $166 \times 100 \times 20$  CV mesh.

On the following figure instantaneous temperature is presented.

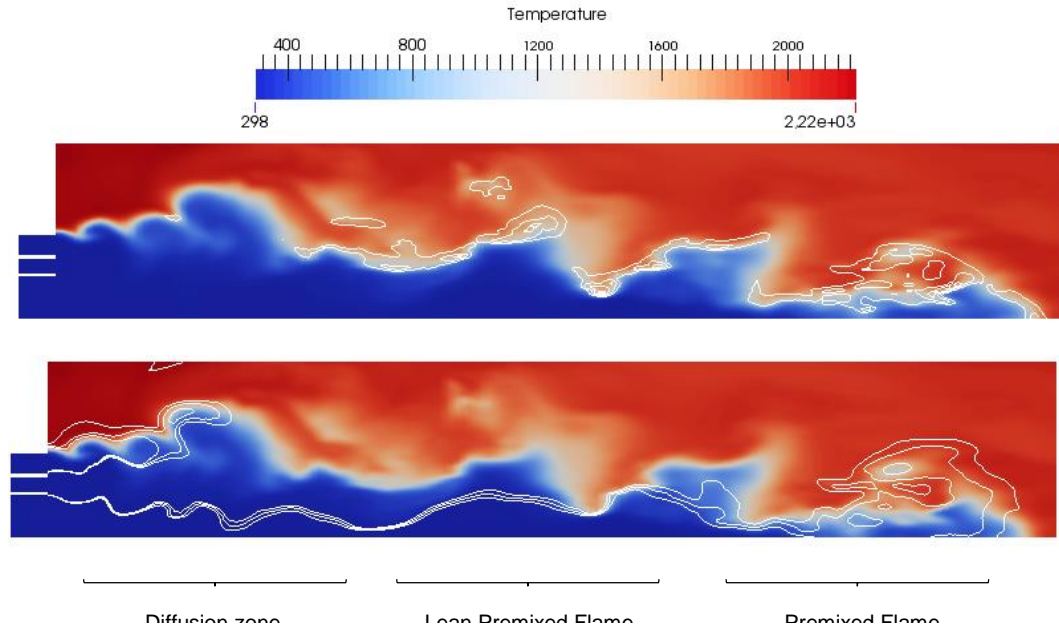


**Figure 40.** Instantaneous field of temperature (K) and rate of production contours (top) and stoichiometric mixture fraction contours  $Z_{st} \pm 0.01$  (bottom) for turbulent  $C_3H_8/\text{Air}$  using a  $166 \times 100 \times 20$  CV mesh.

Different steps on the combustion process are identified through the mixture fraction. Firstly, the fuel and oxygen are mixed in the diffusion zone. Upper this zone a recirculation of hot gases and some fuel appears, which produces small

combustion spots with the air inlet. Secondly, a premixed flame appears with low rates of combustion due to too lean or too rich mixtures. Finally, at the end of the burner, the high diffusion of propane into the oxidizer leads to a premixed flame with high rates and high temperatures. This can be seen on the mixture fraction contours, where the mixture is burned at stoichiometric conditions at the end of the burner.

In section 2.3.2.3 the importance of using a symmetry-preserving scheme is described. This is so important in turbulence, where the non-conservation of the kinetic energy results in a much more dissipative formulation.

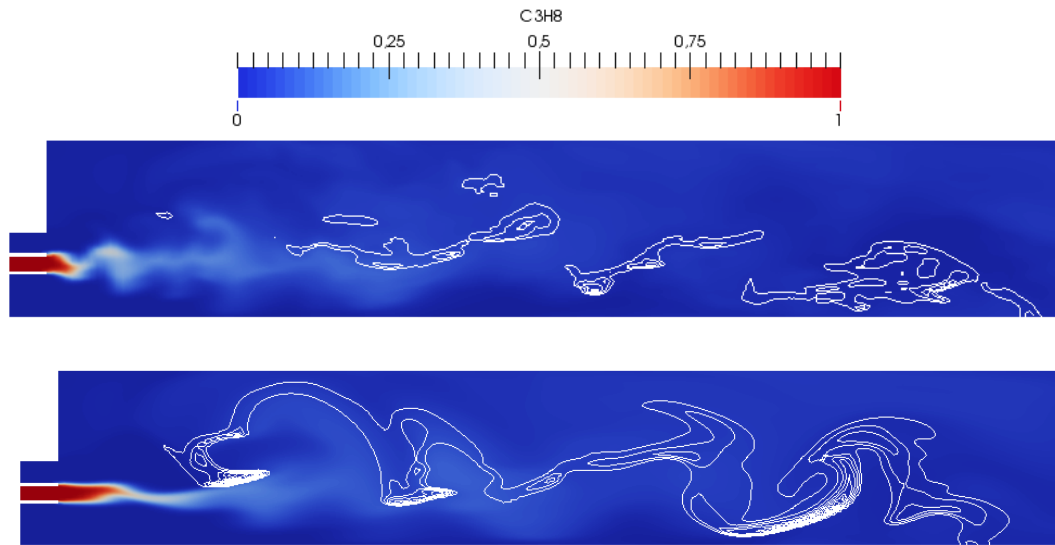


**Figure 41.** Instantaneous field of propane mass fraction and rate of production contours for turbulent  $C_3H_8$ /Air using a  $166 \times 100 \times 20$  CV mesh (SP on top and UDS on bottom).

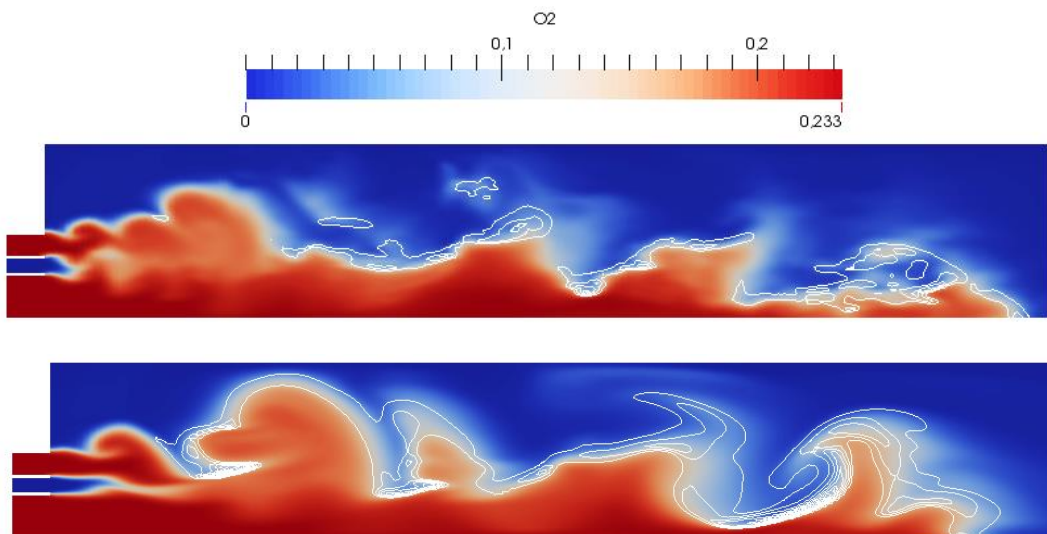


**Figure 42.** Instantaneous field of oxygen mass fraction and rate of production contours for turbulent  $C_3H_8$ /Air using a  $166 \times 100 \times 20$  CV mesh (SP on top and UDS on bottom).

## 4. TURBULENCE MODELLING

---

Two different tests are carried out to compare the influence of the SP in the momentum equations. The first one with a SP scheme and the other one with a UDS (non-conservative) scheme. Both cases use a HDS scheme to solve the scalar equations. As expected, the non-conservative scheme is unable to model correctly the turbulence phenomenon, while the SP scheme conserves kinetic energy and is able to represent accurately more turbulent scales.

## 5. Schedule

The present study has been divided into different tasks, which all of them ensures the finalization of it. Letter T refers to theoretical tasks, C to code implementation and verification tasks and G to general tasks.

A Gantt diagram is used to schedule the development of each tasks, starting at March and concluding at June.

### 5.1. Task Description

In the following section, all tasks with a brief explanation are exposed.

#### **T1. Low Mach Equations**

##### **- T1.1. Governing Equations**

Definition of the governing equations for a low Mach number flow, including the mass, momentum and energy conservation, state equations for ideal gas and its application on open and closed cavities, a description of the projection method and its particularities.

##### **- T1.2. Spatial and Temporal Discretization**

Application of the finite volume method to the governing equations defined on the task before, including the spatial and temporal discretization, numerical schemes and boundaries definition.

#### **C1. Low Mach Equations**

##### **- C1.1. Basic Code Implementation**

Implementation of the main program structure, which includes all functionalities that are not included on the algorithm resolution. This implies processes to export data, variables definition, memory allocation, grid definition among others.

##### **- C1.2. Low Mach Equations Implementation**

Implementation of the low Mach algorithm and also the numerical schemes, the convective – diffusive equation and the stability methods to compute the time step.

##### **- C1.3. Parallel Implementation**

Modify the implemented code to use more than one core and reduce the overall computational time.

## 5. SCHEDULE

---

### - C1.4. Verification

Definition of three tests, which includes boundary conditions, specific variables or numbers per test and a comparison and verification of results.

- C1.4.1 Test – Driven Cavity
- C1.4.2 Test – Heated Cavity
- C1.4.3 Test – Parallel Execution

## T2. Reacting Flows

### - T2.1. Species Characterization

Define the thermodynamic properties, thermochemistry and also chemical kinetics basis of a reacting flow of a mixture gas.

### - T2.2. Chemical Models

Define the simplified chemical mechanisms used to simulate the combustion process.

### - T2.3. Governing Equations

Introduce the governing equations used on reacting flows to control the species transport and also the heat release of different reactions involved into the combustion process.

### - T2.4. Laminar Flames

Introduce the main properties of laminar flames and also the premixed flames and non-premixed flames.

## C2. Reacting Flows

### - C2.1. Species Transport Implementation

Implementation of the species transport equation without reacting flows.

### - C2.2. Thermodynamic Coefficients Implementation

Create a database of multiple properties of different species.

### - C2.3. Chemical Models Implementation

Implementation of the equations to compute a generic chemical mechanism, and also prepare the two models defined for the verification task.

## 5. SCHEDULE

---

### - C2.4. Parallel Implementation

Modify the implemented code to use more than one core to reduce the computational time of the reacting flows algorithm.

### - C2.5. Verification

Definition of tests, which includes the boundary conditions, specific variables or numbers per test and also the comparison and verification of results.

#### ○ C2.5.1 Test –Single Step $CH_4/Air$

#### ○ C2.5.2 Test – Four Step $CH_4/Air$

### T3. Turbulence Modelling

#### - T3.1. Turbulence

Introduction to the turbulence phenomena, the importance of the spatial scales and methods to simulate it.

#### - T3.2. Large Eddy Simulation Models

Define LES equations, the eddy dissipation combustion model, the chemical mechanism used on further tests and also the importance of using the Favre average equations.

### C3. Turbulence Modelling

#### - C3.1. Large Eddy Simulation Implementation

Implementation of LES and Smagorinsky models, the eddy dissipation model.

#### - C3.2. Verification

Definition of test, including boundaries and specific variables. Comparison and verification of the results obtained.

### G1. Report Redaction

This task is done in parallel with other tasks, and mainly consists on the redaction of the present memory to compile all the achieved knowledge.

## 5.2. Gantt Diagram

On the following table, the estimation of hours per task used on the development of the Gantt diagram is exposed. Computational times are not included on the estimations, and it is considered that during the simulations, other tasks are done.

Table 16. Estimation of hours per task scheduled.

<i>Group</i>	<i>Task</i>	<i>Man - hours</i>	<i>Total Time (hours)</i>
T1	T1.1	15	30
	T1.2	15	
C1	C1.1	15	90
	C1.2	50	
	C1.3	15	
	C1.4	10	
T2	T2.1	5	30
	T2.2	5	
	T2.3	15	
	T2.4	5	
C2	C2.1	15	70
	C2.2	15	
	C2.3	25	
	C2.4	5	
	C2.4	10	
T3	T3.1	5	20
	T3.2	15	
C3	C3.1	25	40
	C3.2	15	
G1	-	25	25
<b>Total</b>			<b>305</b>

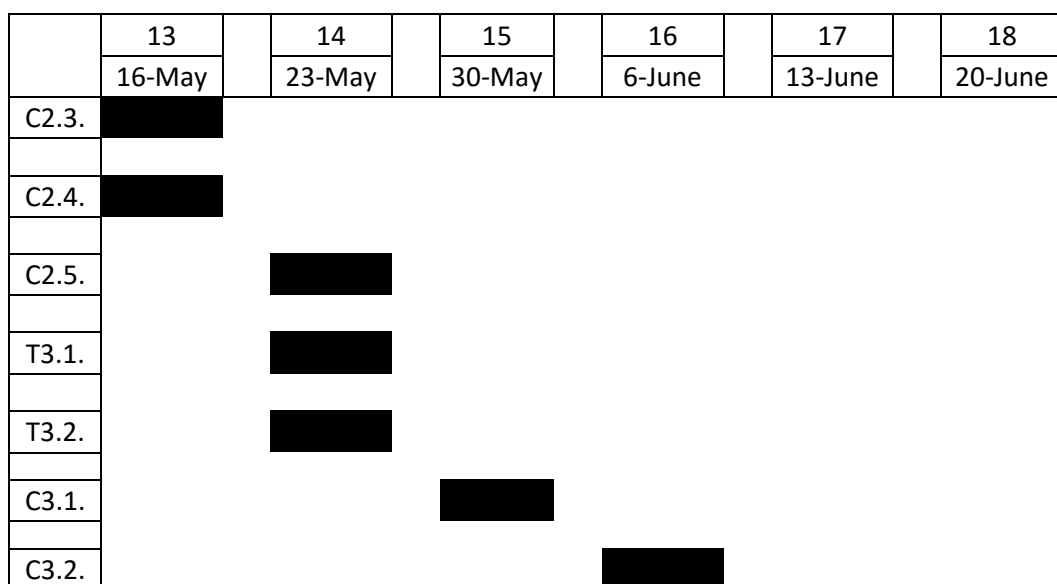
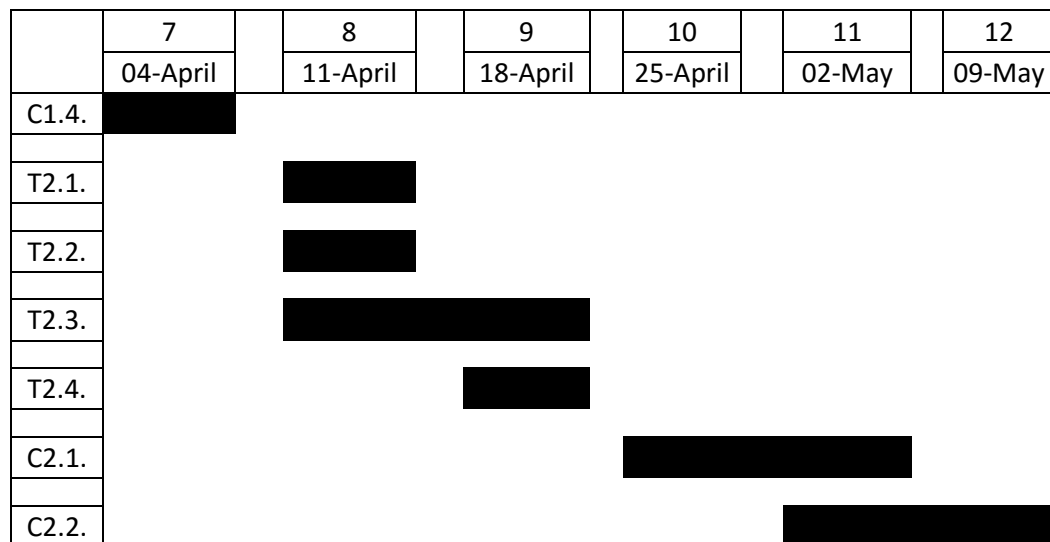
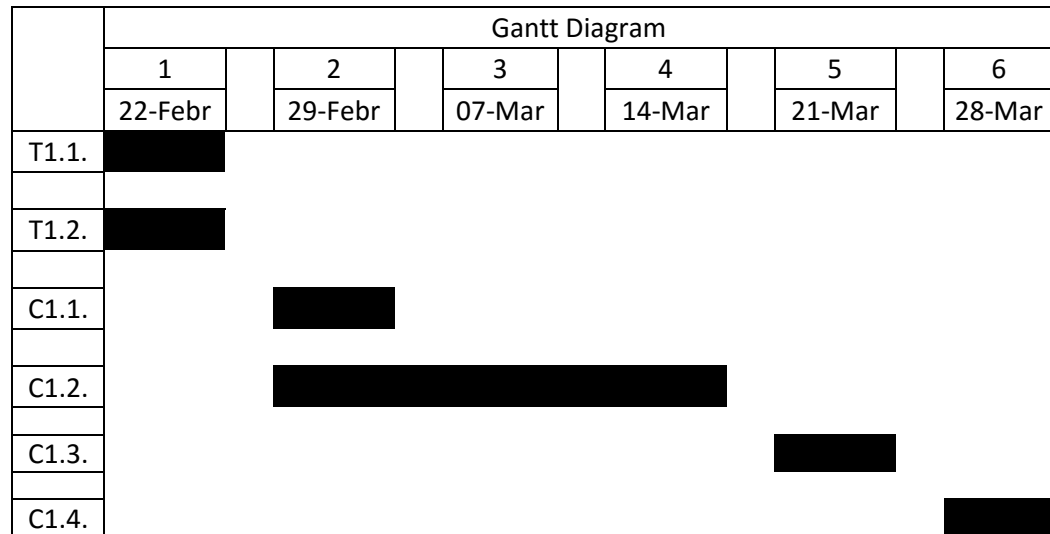


Figure 43. Gantt Diagram.



## 6. Environmental Impact

To analyze the environmental impact of the present study, three different aspects must be differentiated, which are the impact on the development, the processing / post – processing and finally the potential of CFD and reacting flows on the aeronautical field.

The environmental impact during the development phase is reduced to electrical consumption by computers and their peripherals. It includes the development of the code and simulations – tests carried out to verify it. Simulations use high number of cores, which increases the overall power consumption. Taking in account that a simple turbulent combustion simulation takes 72 hours to get reasonable results, it requires about 22 *KWh* per simulation. Therefore, this consumption would be larger if complex geometries are studied, with smooth and small grid sizes and also with complex chemical mechanisms and turbulent flows.

The real environmental impact of this study belongs to its industrial applicability. Utilization of CFD codes to simulate combustion processes and also heat transfers and flow dynamics could reduce real experimentation. Moreover modifications and improvements on designs could be tested without fabrication, with the reduction on costs and contamination due to manufacture processes. This improvement takes relevance in aviation, where experimentation with reactors and turbofan engines implies burning high amounts of fuel (hundreds of liters per hour), construct and maintain special infrastructures and also generate acoustic contamination.

In addition, CFD codes can help engineers to understand the physics of combustion and optimize it. Results could lead to engines with better thrust and specific fuel consumptions, which could reduce the pollution generated by the civil aviation which nowadays takes an important role.

It is interesting to note that usually supercomputers are used to execute complex CFD simulations. Nowadays, these computers consume large amounts of electrical power (thousands of KW), almost all of this energy becomes heat.

## 7. Budget

A budget of the present study is exposed on this section. All human and technological resources, electrical power consumption, hardware and software used on the study development are included on it.

**Table 17.** Cost per resource and final budget of the study.

<i><b>Resource</b></i>	<i><b>Description</b></i>	<i><b>Unit Cost</b></i>	<i><b>Cost (€)</b></i>
Electrical Power	300 W per hour	0.09 €/KWh	10
	Paraview®	Free	0.0
Software	Octave®	Free	0.0
	GNU C++ Compiler	Free	0.0
	Office®	12 €/month	40
	Windows® 10	Free	0.0
	Ubuntu 15.10	Free	0.0
Hardware	Desktop PC	20% of total cost	300
	Laptop PC	20% of total cost	100
Human Resources	305 man-hours	15 €/hour	4575
<b>Total Cost</b>			<b>5025</b>

The final cost of this study is 5025 €.

## 8. Conclusions

A CFD code to simulate laminar and turbulent combustion has been developed. The Low – Mach equations with the species transport equations and chemical kinetics mechanisms are discretized with the finite volume method. A two steps projection method is used as the algorithm of resolution.

Different tests to verify the implemented equations are exposed. The first ones are used to verify the momentum and energy equations, and also to check the parallel implementation. Two additional tests are performed to verify the simulation of laminar and turbulent flames. The last one is computed using the LES method with the Smagorinsky model. In both cases the mass fractions, temperatures and rates of reactions are exposed.

From the heated cavity the importance of using variable properties to obtain realistic results is evidenced. Variable density modifies the thickness of the boundary layers and the recirculation patterns, in particular near the walls. This test is also used to check the numerical schemes, where all of them show similar results.

From the laminar combustion tests, it is seen that the four steps chemical mechanism is able to get a good approximation of temperature profiles, but still presents an important lack of accuracy on the mass fraction values, specifically the  $CO_2$ . The prediction of the flame thickness is important, which is very helpful to set a correct grid size. The single step chemical mechanism offers poor results in comparison with the first one, and the execution times required are quite similar.

From the turbulent test, it is seen that the application of the Smagorinsky model and the EDM to introduce the heat released by the Kolmogorov scales is useful to obtain a good estimation of the flow pattern. Results are quite similar with the experimental ones and differ slightly from Howard et. al. [17] ones. The effect of different numerical schemes is also analyzed. SP schemes on the momentum equation introduces more spatial scales than the UDS. This reduces the fluctuation part on UDS scheme which leads to reduced integration times to obtain the mean and fluctuation part of the variables. Even so, the accuracy on the description of the flow behavior is reduced.

On the other hand, the EDM has shown an important dependence on the  $C_\mu$ , where larger values tends to increase the combustion and lower ones to extinguish it. Different tests show that  $C_\mu = 0.07$  seems to be adequate for the present case and accurate results are obtained with it.

## 9. Further Developments

The study developed is only a first approach to simulate combustion processes. With the aim of applying it to aeronautical processes, different improvements would be needed.

- Using uniform meshes imposes a very restrictive limitation on burner geometries. Typical burners present some irregularities on the chamber and also complicated injection geometries. It becomes clear that further steps must involve unstructured meshes.
- Implement chemical mechanisms with more species and reactions, with the aim of increasing the accuracy on laminar flames.
- The effects of numerical schemes into turbulent flows has been shown. Further developments could include more and an exhaustive comparison between them.
- In this study only the Smagorinsky model to compute the turbulent viscosity has been implemented. This model is known to introduce too much diffusion, which eliminates more scales than the desired ones. There are other models that could offer better results, such as Wale or Dynamic Smagorinsky.
- Repeat the 3D turbulent combustion case on multiple grid sizes and establish a relation between accuracy and mesh resolution.
- Radiation has been introduced on the present study without its application. In flames with large temperatures, this could take an important role on the energy transport. Further developments must take this term into account.
- To generalize the implementation, the introduction of the corrector velocities for the molecular diffusion could be interesting instead of using the nitrogen (diluent) to absorb all the inconsistencies on the species mass conservation.

## Bibliography

- [1] K. Liu and R. H. Pletcher, "A fractional step method for solving the compressible Navier-Stokes equations," *Journal of Computational Physics*, vol. 226, pp. 1930-1951, 5 7 2007.
- [2] L. Bamdad and P. Miltiadis V., "Time-accurate calculation of variable density flows with strong temperature gradients and combustion," *Journal of Computational Physics*, vol. 212, pp. 218-246, 10 8 2006.
- [3] A. W. Cook and J. J. Riley, "Direct numerical simulation of a turbulent reactive plume on a parallel computer," *Journal of computational physics*, vol. 129, pp. 263-283, 20 5 1996.
- [4] A. Tyliczszak, "Projection method for high-order compact schemes for low Mach number flows in enclosures," *International Journal of Numerical Methods for Heat & Fluid Flow*, vol. 24, no. 5, pp. 1141-1174, 2013.
- [5] S. V. Patankar, *Numerical heat transfer and fluid flow*, New York: Hemisphere Publishing Corporation, 1980.
- [6] P. M, R. Kessler and G. Scheuerer, "Comparison of finite-volume numerical methods with staggered and colocated grids," *Computers & Fluids*, vol. 16, no. 4, pp. 389-403, 1988.
- [7] F. X. Trias, O. Lehmkuhl, A. Oliva and C. D. Pérez-Segarra, "Symmetry-preserving discretization of Navier-Stokes equations on colocated unstructured grids," *Journal of Computational Physics*, vol. 258, pp. 246-267, 2014.
- [8] U. Ghia, K. N. Ghia and C. T. Shin, "High-Re solutions for incompressible flow using the Navier - Stokes equations and multigrid method," *Journal of computational physics*, vol. 48, pp. 387-411, 1982.
- [9] J. Vierendeels, B. Merci and E. Dick, "Benchmark solutios for the natural convective heat transfer problem in a square cavity with large horizontal temperature differences," *International journal of numerical methods for heat & fluid flow*, vol. 13, no. 8, pp. 1057-1078, 2003.

- [10] T. Poinso and D. Veynante, Theoretical and numerical combustion, Toulouse: Edwards, 2001.
- [11] B. J. McBride, S. Gordon and M. A. Reno, "Coefficients for Calculating Thermodynamic and Transport Properties of Individual Species," Cleveland, 1993.
- [12] J. W. P. and L. R. P., "Global Reaction Schemes for Hydrocarbon Combustion," *Combustion and Flame*, no. 73, pp. 233-249, 1988.
- [13] CTTC, "Introducción a la formulación matemática de la combustion de gases reactivos," Terrassa.
- [14] B. Fiorina, R. Baron, O. Gicquel, D. Thevenin, S. Carpentier and N. Darabiha, "Modelling non-adiabatic partially premixed flames using flame-prolongation of ILDM," *Combustion Theory and Modelling*, vol. 3, no. 7, pp. 449-470, 2014.
- [15] H. Pitsch, "Large - Eddy Simulation of Turbulent Combustion," *Annual Review of Fluid Mechanics*, no. 38, pp. 453-482, 2006.
- [16] D. C. Wilcox, Turbulence modeling for CFD, La Cañada: Griffin Printing, 1993.
- [17] H. R. J. A. and D. Toporov, "The eddy dissipation combustion model developed for large eddy simulation," Aveiro.
- [18] J. Smagorinsky, "General circulation experiments with the primitive equations, the basic experiment," *Monthly weather review*, vol. 91, no. 3, pp. 100-164, 1963.
- [19] C. D. Perez-Segarra, C. Farre, J. Cadafalch and A. Oliva, "Analysis of different numerical schemes for the resolution of convection - diffusion equations using finite-volume methods on three-dimensional unstructured grids," *Numerical Heat Transfer*, no. 49, pp. 333-350, 2006.
- [20] B. F. Magnussen, "The eddy dissipation concept a bridge between science and technology," Lisbon, 2005.
- [21] J. P. Lieger, "Simulations numeriques des instabilites de combustion dans les foyers aeronatiques," Institut National Polytechnique de Toulouse, Toulouse, 2001.

## Appendix A – Coefficients for Thermodynamic Properties

On the following tables the thermodynamic coefficients of species that are used on numerical tests are exposed.

**Table 18.** Methane (CH<sub>4</sub>) coefficients from 200 - 1000 K.

	0	1	2	3	4	5
<i>a</i>	$0.5149876130 \cdot 10$	$-0.1367097880 \cdot 10^{-1}$	$0.4918005990 \cdot 10^{-4}$	$-0.484743026010 \cdot 10^{-7}$	$0.1666939560 \cdot 10^{-10}$	$-0.1024664760 \cdot 10^5$
<i>b</i>	$-0.2230715913 \cdot 10^2$	$0.3569542093 \cdot 10$	$-0.38749203$	$0.1712461411 \cdot 10^{-1}$	-	-
<i>c</i>	$0.1793259165 \cdot 10$	$-0.4960294457 \cdot 10$	$0.1032808843 \cdot 10$	$-0.5633567903 \cdot 10^{-1}$	-	-

**Table 19.** Methane (CH<sub>4</sub>) coefficients from 1000 - 5000 K.

	0	1	2	3	4	5
<i>a</i>	$0.7485149500 \cdot 10^{-1}$	$0.1339094670 \cdot 10^{-1}$	$-0.5732858090 \cdot 10^{-5}$	$0.1222925350 \cdot 10^{-8}$	$-0.1018152300 \cdot 10^{-12}$	$-0.9468344590 \cdot 10^4$
<i>b</i>	$-0.2230715913 \cdot 10^2$	$0.3569542093 \cdot 10$	$-0.3874920393$	$0.1712461411 \cdot 10^{-1}$	-	-
<i>c</i>	$0.1793259165 \cdot 10$	$-0.4960294457 \cdot 10$	$0.1032808843 \cdot 10$	$-0.5633567903 \cdot 10^{-1}$	-	-

**Table 20.** Oxygen (O<sub>2</sub>) coefficients from 200 - 1000 K.

	0	1	2	3	4	5
<i>a</i>	$0.3782456360 \cdot 10$	$-0.2996734160 \cdot 10^{-2}$	$0.9847302010 \cdot 10^{-5}$	$-0.9681295090 \cdot 10^{-8}$	$0.3243728370 \cdot 10^{-11}$	$-0.1063943560 \cdot 10^4$
<i>b</i>	$-0.1946067566 \cdot 10^2$	$0.2678088349 \cdot 10$	$-0.2721592408$	$0.1214173233 \cdot 10^{-1}$	-	-
<i>c</i>	$-0.1344962361 \cdot 10^2$	$0.2890477542 \cdot 10$	$-0.2709591162$	$0.1152570281 \cdot 10^{-1}$	-	-

**Table 21.** Oxygen (O<sub>2</sub>) coefficients from 1000 - 5000 K.

	0	1	2	3	4	5
<i>a</i>	$0.3282537840 \cdot 10$	$0.1483087540 \cdot 10^{-2}$	$-0.7579666690 \cdot 10^{-6}$	$0.2094705550 \cdot 10^{-9}$	$-0.2167177940 \cdot 10^{-13}$	$-0.1088457720 \cdot 10^4$
<i>b</i>	$-0.1946067566 \cdot 10^2$	$0.2678088349 \cdot 10$	$-0.2721592408$	$0.1214173233 \cdot 10^{-1}$	-	-
<i>c</i>	$-0.1344962361 \cdot 10^2$	$0.2890477542 \cdot 10$	$-0.2709591162$	$0.1152570281 \cdot 10^{-1}$	-	-

**Table 22.** Carbon Monoxide (CO) coefficients from 200 - 1000 K.

	0	1	2	3	4	5
<i>a</i>	$0.3579533470 \cdot 10$	$-0.6103536800 \cdot 10^{-3}$	$0.1016814330 \cdot 10^{-5}$	$0.9070058840 \cdot 10^{-9}$	$-0.9044244990 \cdot 10^{-12}$	$-0.1434408600 \cdot 10^5$
<i>b</i>	$-0.1891819775 \cdot 10^2$	$0.2400975158 \cdot 10$	$-0.2357717790$	$0.1054820948 \cdot 10^{-1}$	-	-
<i>c</i>	$0.3641755785$	$-0.3154801253 \cdot 10$	$0.6020483455$	$-0.3032714733 \cdot 10^{-1}$	-	-

**Table 23.** Carbon Monoxide (CO) coefficients from 1000 - 5000 K.

	0	1	2	3	4	5
<i>a</i>	$0.2715185610 \cdot 10$	$0.2062527430 \cdot 10^{-2}$	$-0.9988257710 \cdot 10^{-6}$	$0.2300530080 \cdot 10^{-9}$	$-0.2036477160 \cdot 10^{-13}$	$-0.1415187240 \cdot 10^4$
<i>b</i>	$-0.1891819775 \cdot 10^2$	$0.2400975158 \cdot 10$	$-0.2357717790$	$0.1054820948 \cdot 10^{-1}$	-	-
<i>c</i>	$0.3641755785$	$-0.3154801253 \cdot 10$	$0.6020483455$	$-0.3032714733 \cdot 10^{-1}$	-	-

**Table 24.** Carbon dioxide (CO<sub>2</sub>) coefficients from 200 - 1000 K.

	0	1	2	3	4	5
<i>a</i>	$0.2356773520 \cdot 10$	$0.8984596770 \cdot 10^{-2}$	$-0.7123562690 \cdot 10^{-5}$	$0.2459190220 \cdot 10^{-8}$	$-0.1436995480 \cdot 10^{-12}$	$-0.4837196970 \cdot 10^5$
<i>b</i>	$-0.2627315808 \cdot 10^2$	$0.5130426196 \cdot 10$	$-0.5724284704$	$0.2440888722 \cdot 10^{-1}$	-	-
<i>c</i>	$-0.2286363338 \cdot 10^2$	$0.5875667874 \cdot 10$	$-0.5677982250$	$0.2031670239 \cdot 10^{-1}$	-	-

**Table 25.** Carbon dioxide (CO<sub>2</sub>) coefficients from 1000 - 5000 K.

	0	1	2	3	4	5
<i>a</i>	$0.3857460290 \cdot 10$	$0.4414370260 \cdot 10^{-2}$	$-0.2214814040 \cdot 10^{-5}$	$0.5234901880 \cdot 10^{-9}$	$-0.4720841640 \cdot 10^{-13}$	$-0.4875916600 \cdot 10^5$
<i>b</i>	$-0.2627315808 \cdot 10^2$	$0.5130426196 \cdot 10$	$-0.5724284704$	$0.2440888722 \cdot 10^{-1}$	-	-
<i>c</i>	$-0.2286363338 \cdot 10^2$	$0.5875667874 \cdot 10$	$-0.5677982250$	$0.2031670239 \cdot 10^{-1}$	-	-

**Table 26.** Water (H<sub>2</sub>O) coefficients from 200 - 1000 K.

	0	1	2	3	4	5
<i>a</i>	$0.4198640560 \cdot 10$	$-0.2036434100 \cdot 10^{-2}$	$0.6520402110 \cdot 10^{-5}$	$-0.5487970620 \cdot 10^{-8}$	$0.1771978170 \cdot 10^{-11}$	$-0.3029372670 \cdot 10^5$
<i>b</i>	$-0.1286013492 \cdot 10^{-2}$	$-0.1377850379 \cdot 10$	$0.4213981638$	$-0.2414423056 \cdot 10^{-1}$	-	-
<i>c</i>	$0.1185254026 \cdot 10^2$	$-0.8965822807 \cdot 10$	$0.1528828068 \cdot 10$	$-0.7590175979 \cdot 10^{-1}$	-	-

**Table 27.** Water (H<sub>2</sub>O) coefficients from 1000 - 5000 K.

	0	1	2	3	4	5
<i>a</i>	$0.3033992490 \cdot 10$	$0.2176918040 \cdot 10^{-2}$	$-0.1640725180 \cdot 10^{-6}$	$-0.9704198700 \cdot 10^{-10}$	$0.1682009920 \cdot 10^{-13}$	$-0.3000429710 \cdot 10^5$
<i>b</i>	$-0.1286013492 \cdot 10^{-2}$	$-0.1377850379 \cdot 10$	$0.4213981638$	$-0.2414423056 \cdot 10^{-1}$	-	-
<i>c</i>	$0.1185254026 \cdot 10^2$	$-0.8965822807 \cdot 10$	$0.1528828068 \cdot 10$	$-0.7590175979 \cdot 10^{-1}$	-	-

**Table 28.** Hydrogen (H<sub>2</sub>) coefficients from 200 - 1000 K.

	0	1	2	3	4	5
<i>a</i>	$0.2344331120 \cdot 10$	$0.7980520750 \cdot 10^{-2}$	$-0.1947815100 \cdot 10^{-4}$	$0.2015720940 \cdot 10^{-7}$	$-0.7376117610 \cdot 10^{-11}$	$-0.9179351730 \cdot 10^4$
<i>b</i>	$-0.1614293964 \cdot 10^2$	$0.1003491326 \cdot 10$	$-0.5016044555 \cdot 10^{-1}$	$0.2330995224 \cdot 10^{-2}$	-	-
<i>c</i>	$-0.2277096638 \cdot 10$	$-0.4674267764$	$0.1156734789$	$-0.2596025563 \cdot 10^{-2}$	-	-

**Table 29.** Hydrogen (H<sub>2</sub>) coefficients from 1000 - 5000 K.

	0	1	2	3	4	5
--	---	---	---	---	---	---



$a$	$0.3337279200 \cdot 10$	$-0.4940247310 \cdot 10^{-4}$	$0.4994567780 \cdot 10^{-6}$	$-0.1795663940 \cdot 10^{-9}$	$0.2002553760 \cdot 10^{-13}$	$-0.9501589220 \cdot 10^3$
$b$	$-0.1614293964 \cdot 10^2$	$0.1003491326 \cdot 10$	$-0.5016044555 \cdot 10^{-1}$	$0.2330995224 \cdot 10^{-2}$	-	-
$c$	$-0.2277096638 \cdot 10$	$-0.4674267764$	$0.1156734789$	$-0.2596025563 \cdot 10^{-2}$	-	-

**Table 30.** Nitrogen (N<sub>2</sub>) coefficients from 200 - 1000 K.

	$0$	$1$	$2$	$3$	$4$	$5$
$a$	$0.3298677000 \cdot 10$	$0.1408240400 \cdot 10^{-2}$	$-0.3963222000 \cdot 10^{-5}$	$0.5641515000 \cdot 10^{-8}$	$-0.2444854000 \cdot 10^{-11}$	$-0.102089990 \cdot 10^4$
$b$	$-0.1886822179 \cdot 10^2$	$0.2388167036 \cdot 10$	$-0.2341208183$	$0.1047727173 \cdot 10^{-1}$	-	-
$c$	$0.1417117599 \cdot 10$	$-0.3528374680 \cdot 10$	$0.6455829015$	$-0.3194413600 \cdot 10^{-1}$	-	-

**Table 31.** Nitrogen (N<sub>2</sub>) coefficients from 1000 - 5000 K.

	$0$	$1$	$2$	$3$	$4$	$5$
$a$	$0.2926640000 \cdot 10$	$0.1487976800 \cdot 10^{-2}$	$-0.5684760000 \cdot 10^{-6}$	$0.1009703800 \cdot 10^{-9}$	$-0.6753351000 \cdot 10^{-14}$	$-0.922797700 \cdot 10^3$
$b$	$-0.1886822179 \cdot 10^2$	$0.2388167036 \cdot 10$	$-0.2341208183$	$0.1047727173 \cdot 10^{-1}$	-	-
$c$	$0.1417117599 \cdot 10$	$-0.3528374680 \cdot 10$	$0.6455829015$	$-0.3194413600 \cdot 10^{-1}$	-	-

Coefficients  $a_6$  used on the entropy computation are described on the following table.

**Table 32.** Coefficients for all species used on the entropy equation for 200 – 100 K (1) and 1000 – 5000 K (2).

	$CH_4$	$O_2$	$CO$	$CO_2$	$H_2O$	$H_2$	$N_2$
$a_{1,6}$	$-0.4641303760 \cdot 10$	$0.3657675730 \cdot 10$	$0.3508409280 \cdot 10$	$0.9901052220 \cdot 10$	$-0.8490322080$	$0.6830102380$	$0.3950372000 \cdot 10$
$a_{2,6}$	$0.1843731800 \cdot 10^2$	$0.5453231290 \cdot 10$	$0.7818687720 \cdot 10$	$0.2271638060 \cdot 10$	$0.4966770100$	$-0.3205023310 \cdot 10$	$0.5980528000 \cdot 10$